CrossMark

Migration and Evolution of giant ExoPlanets (MEEP). I. Nine Newly Confirmed Hot Jupiters from the TESS Mission

Jack Schulte[1], Joseph E. Rodriguez[1], Allyson Bieryla[2], Samuel N. Quinn[2], Karen A. Collins[2], Samuel W. Yee[2,3,50], Andrew C. Nine[4,5], Melinda Soares-Furtado[4,6], David W. Latham[2], Jason D. Eastman[2], Khalid Barkaoui[7,8,9], David R. Ciardi[10], Diana Dragomir[11], Mark E. Everett[12], Steven Giacalone[13,51], Ismael Mireles[11], Felipe Murgas[9,14], Norio Narita[9,15,16], Avi Shporer[6], Ivan A. Strakhov[17], Stephanie Striegel[18,19], Martin Vaňko[20], Noah Vowell[1], Gavin Wang[21], Carl Ziegler[22], Michael Bellaver[1], Paul Benni[23], Serge Bergeron[24], Henri M. J. Boffin[25], César Briceño[26], Catherine A. Clark[10,27], Kevin I. Collins[28], Jerome P. de Leon[29], Courtney D. Dressing[30], Phil Evans[31], Emma Esparza-Borges[9,14], Jeremy Fedewa[1], Akihiko Fukui[9,15], Tianjun Gan[32], Ivan S. Gerasimov[17], Joel D. Hartman[3], Holden Gill[30], Michaël Gillon[7], Keith Horne[33], Ferran Grau Horta[34], Steve B. Howell[19], Keisuke Isogai[29,35], Emmanuël Jehin[36], Jon M. Jenkins[19], Raine Karjalainen[37], John F. Kielkopf[38], Kathryn V. Lester[19], Colin Littlefield[19,39], Michael B. Lund[10], Andrew W. Mann[40], Mason McCormack[41], Edward J. Michaels[42], Shane Painter[1], Enric Palle[9,14], Hannu Parviainen[9,14], David-Michael Peterson[1], Francisco J. Pozuelos[7,43], Zachary Raup[44], Phillip Reed[44], Howard M. Relles[2], George R. Ricker[6], Arjun B. Savel[45], Richard P. Schwarz[2], S. Seager[6,8,46], Ramotholo Sefako[47], Gregor Srdoc[48], Chris Stockdale[49], Hannah Sullivan[1], Mathilde Timmermans[7], and Joshua N. Winn[3]

[1] Center for Data Intensive and Time Domain Astronomy, Department of Physics and Astronomy, Michigan State University, East Lansing, MI 48824, USA; jschulte@msu.edu
[2] Center for Astrophysics | Harvard & Smithsonian, 60 Garden Street, Cambridge, MA 02138, USA
[3] Department of Astrophysical Sciences, Princeton University, 4 Ivy Lane, Princeton, NJ 08544, USA
[4] Department of Astronomy, University of Wisconsin-Madison, 475 N. Charter Street, Madison, WI 53706, USA
[5] Department of Physics and Astronomy, Carleton College, 215 Goodsell Circle, Northfield, MN 55057, USA
[6] Department of Physics and Kavli Institute for Astrophysics and Space Research, Massachusetts Institute of Technology, Cambridge, MA 02139, USA
[7] Astrobiology Research Unit, Université de Liège, 19C Allée du 6 Août, 4000 Liège, Belgium
[8] Department of Earth, Atmospheric and Planetary Science, Massachusetts Institute of Technology, 77 Massachusetts Avenue, Cambridge, MA 02139, USA
[9] Instituto de Astrofísica de Canarias (IAC), 38200 La Laguna, Tenerife, Spain
[10] NASA Exoplanet Science Institute-Caltech/IPAC, Pasadena, CA 91125, USA
[11] Department of Physics and Astronomy, University of New Mexico, 210 Yale Boulevard NE, Albuquerque, NM 87106, USA
[12] NSF's National Optical-Infrared Astronomy Research Laboratory, 950 N. Cherry Avenue, Tucson, AZ 85719, USA
[13] Department of Astronomy, California Institute of Technology, Pasadena, CA 91125, USA
[14] Deptartamento de Astrofísica, Universidad de La Laguna (ULL), 38206 La Laguna, Tenerife, Spain
[15] Komaba Institute for Science, The University of Tokyo, 3-8-1 Komaba, Meguro, Tokyo 153-8902, Japan
[16] Astrobiology Center, 2-21-1 Osawa, Mitaka, Tokyo 181-8588, Japan
[17] Sternberg Astronomical Institute, Lomonosov Moscow State University, Universitetsky pr. 13, Moscow 119234, Russia
[18] SETI Institute, Mountain View, CA 94043, USA
[19] NASA Ames Research Center, Moffett Field, CA 94035, USA
[20] Astronomical Institute, Slovak Academy of Sciences, 059 60 Tatranská Lomnica, Slovakia
[21] Tsinghua International School, Beijing 100084, People's Republic of China
[22] Department of Physics, Engineering and Astronomy, Stephen F. Austin State University, 1936 North Street, Nacogdoches, TX 75962, USA
[23] Acton Sky Portal (private observatory), Acton, MA USA
[24] American Association of Variable Star Observers, 185 Alewife Brook Parkway, Suite 410, Cambridge, MA 02138, USA
[25] European Southern Observatory, D-85748 Garching, Germany
[26] Cerro Tololo Inter-American Observatory/NSF's NOIRLab, Casilla 603, La Serena, Chile
[27] Jet Propulsion Laboratory, California Institute of Technology, Pasadena, CA 91109, USA
[28] George Mason University, 4400 University Drive, Fairfax, VA, 22030, USA
[29] Department of Multi-Disciplinary Sciences, Graduate School of Arts and Sciences, The University of Tokyo, 3-8-1 Komaba, Meguro, Tokyo 153-8902, Japan
[30] Department of Astronomy, University of California, Berkeley, Berkeley, CA 94720-3411, USA
[31] El Sauce Observatory, Coquimbo Province, Chile
[32] Department of Astronomy, Tsinghua University, Beijing 100084, People's Republic of China
[33] SUPA Physics and Astronomy, University of St. Andrews, Fife, KY16 9SS Scotland, UK
[34] Observatori de Ca l'Ou, Carrer de dalt 18, Sant Martí Sesgueioles 08282, Barcelona, Spain
[35] Okayama Observatory, Kyoto University, 3037-5 Honjo, Kamogatacho, Asakuchi, Okayama 719-0232, Japan
[36] Space Sciences, Technologies and Astrophysics Research (STAR) Institute, Université de Liège, Allée du 6 Août 19C, B-4000 Liège, Belgium
[37] Astronomical Institute of the Czech Academy of Sciences, Fričova 298, 25165 Ondřejov, Czech Republic
[38] Department of Physics and Astronomy, University of Louisville, Louisville, KY 40292, USA
[39] Bay Area Environmental Research Institute, Moffett Field, CA 94035, USA
[40] Department of Physics and Astronomy, The University of North Carolina at Chapel Hill, Chapel Hill, NC 27599-3255, USA
[41] Department of Astronomy and Astrophysics, 5640 South Ellis Avenue, University of Chicago, Chicago, IL 60637, USA
[42] Waffelow Creek Observatory
[43] Instituto de Astrofísica de Andalucía (IAA-CSIC), Glorieta de la Astronomía s/n, 18008 Granada, Spain
[44] Department of Physical Sciences, Kutztown University, Kutztown, PA 19530, USA
[45] Department of Astronomy, University of Maryland, College Park, College Park, MD 20742, USA
[46] Department of Aeronautics and Astronautics, MIT, 77 Massachusetts Avenue, Cambridge, MA 02139, USA
[47] South African Astronomical Observatory, P.O. Box 9, Observatory, 7935, Cape Town, South Africa
[48] Kotizarovci Observatory, Sarsoni 90, 51216 Viskovo, Croatia

[49] Hazelwood Observatory, Australia

Abstract

Hot Jupiters were many of the first exoplanets discovered in the 1990s, but in the decades since their discovery the mysteries surrounding their origins have remained. Here we present nine new hot Jupiters (TOI-1855 b, TOI-2107 b, TOI-2368 b, TOI-3321 b, TOI-3894 b, TOI-3919 b, TOI-4153 b, TOI-5232 b, and TOI-5301 b) discovered by NASA's TESS mission and confirmed using ground-based imaging and spectroscopy. These discoveries are the first in a series of papers named the Migration and Evolution of giant ExoPlanets survey and are part of an ongoing effort to build a complete sample of hot Jupiters orbiting FGK stars, with a limiting Gaia *G*-band magnitude of 12.5. This effort aims to use homogeneous detection and analysis techniques to generate a set of precisely measured stellar and planetary properties that is ripe for statistical analysis. The nine planets presented in this work occupy a range of masses ($0.55 M_J < M_P < 3.88 M_J$) and sizes ($0.967 R_J < R_P < 1.438 R_J$) and orbit stars that have an effective temperature in the range of $5360\,\mathrm{K} < T_{\mathrm{eff}} < 6860\,\mathrm{K}$ with Gaia *G*-band magnitudes ranging from 11.1 to 12.7. Two of the planets in our sample have detectable orbital eccentricity: TOI-3919 b ($e = 0.259^{+0.033}_{-0.036}$) and TOI-5301 b ($e = 0.33^{+0.11}_{-0.10}$). These eccentric planets join a growing sample of eccentric hot Jupiters that are consistent with high-eccentricity tidal migration, one of the three most prominent theories explaining hot Jupiter formation and evolution.

Unified Astronomy Thesaurus concepts: Exoplanet astronomy (486); Exoplanet migration (2205); Exoplanet detection methods (489); Exoplanets (498); Transits (1711); Radial velocity (1332); Direct imaging (387)

1. Introduction

The first exoplanet discovered around a main-sequence star, 51 Pegasi b (Mayor & Queloz 1995), immediately had an impact on the fundamental theories of planet formation and evolution. 51 Pegasi b, like many of the planets that followed, is a hot Jupiter (HJ), or a gas giant planet ($>0.25 M_J$) orbiting its host star with a period less than 10 days (Dawson & Johnson 2018). Now, close to 30 yr later, over 5500 additional planets have been confirmed, approximately 10% of which are HJs. The rapid discovery of HJs has prompted questions about how these giant planets, with orbits far more compact than any in our solar system, came to be. Several theories have been proposed to explain the preponderance of short-period giant planets, which we group into three categories: in situ formation (Batygin et al. 2016), gas-disk migration (Goldreich & Tremaine 1980; Lin & Papaloizou 1986), and high-eccentricity tidal migration (e.g., Kozai 1962; Lidov 1962; Rasio & Ford 1996; Naoz 2016).

The plausibility of in situ formation, the idea that giant planets can form in their present-day orbital configurations and not require large-scale migration, has been debated throughout the past two decades (Rafikov 2005, 2006; Lee et al. 2014; Boley et al. 2016; Poon et al. 2021). The majority of the currently accepted literature suggests that in situ formation is unlikely to be the dominant mechanism to form HJs, as it would require a rapid buildup of ~10 Earth masses ($M_\oplus$) of solids in a region of the protoplanetary disk where the feeding zones are tiny (Dawson & Johnson 2018). Additionally, the cores that form would not likely be able to accrete enough gas to form an HJ before the dissipation of the gas disk (Lee et al. 2014; Dawson & Johnson 2018). Batygin et al. (2016) argued that rapid gas accretion onto planets with masses between 10 and 20 $M_\oplus$ is possible but that HJs that form in situ should be

accompanied by low-mass planets on short periods, a scenario that has proven to be rare (Huang et al. 2016).

If in situ formation is not the dominant mechanism to produce HJs, then there must be some mechanisms for giant planets to undergo large-scale migration from orbits beyond ~3 au to less than ~0.1 au. The currently favored pathways for this large-scale migration are gas-disk migration, where the planet transfers its orbital energy and angular momentum to the protoplanetary disk (Goldreich & Tremaine 1980; Lin & Papaloizou 1986), and high-eccentricity tidal migration, where the planet exchanges angular momentum with another planet or star, exciting the planet's eccentricity to be later circularized on a much smaller orbit as a consequence of tidal interactions with the host star (Rasio & Ford 1996; Fabrycky & Tremaine 2007). Each of these mechanisms is expected to generate different observable outcomes in planetary systems that have undergone migration. Gas-disk migration does not typically excite the orbital eccentricities or misalign the orbits of the migrating planets, whereas planets that have undergone high-eccentricity tidal migration may still have observable eccentric or misaligned orbits that are remnants of their migration (Dawson & Johnson 2018). Additionally, high-eccentricity tidal migration typically destabilizes the orbits of nearby planets, leading to the preponderance of isolated HJs (Huang et al. 2016), while gas-disk migration is more quiescent, enabling nearby companions to survive (Becker et al. 2015; Vanderburg et al. 2017).

This article is the first in connection with a survey intended to construct a magnitude-limited, complete sample of HJs and warm Jupiters with precisely measured masses, radii, semimajor axes, and eccentricities. This set of parameters will be useful for future efforts to understand the HJ population and constrain the migration pathways of giant planets. Our survey, which we name the Migration and Evolution of giant ExoPlanets (MEEP) survey, is joining other efforts (Rodriguez et al. 2019, 2021; Ikwut-Ukwa et al. 2022; Yee et al. 2022; Rodriguez et al. 2023; Yee et al. 2023) to build such a catalog of parameters using data from the Transiting Exoplanet Survey Satellite (TESS; Ricker et al. 2015) and homogeneous analysis techniques, to ensure that statistical studies can be performed

---

on the sample with a good understanding of the selection biases. This sample will be constrained by the host star brightness to ensure that radial velocity (RV) observations yield a precise mass and eccentricity, and so only planets with host star Gaia G-band magnitudes brighter than 12.5 will be included. Yee et al. (2021) find that there are likely roughly $300-400$ discoverable transiting HJs orbiting FGK stars brighter than $G = 12.5$ mag, and while <300 of these have been confirmed so far, TESS should be able to detect nearly all of the remaining undiscovered HJs. With a complete sample of HJs orbiting bright FGK stars, we will be able to confidently explore the distribution of planetary and stellar parameters of HJ-hosting systems, nailing down the occurrence rate of HJs around Sun-like stars and probing the likelihood of each formation and evolution mechanism by comparing population synthesis models to the observed distribution of orbital eccentricity and orbital period. Ikwut-Ukwa et al. (2022) found tentative evidence for multiple, separate distributions in mass$-$period space in the incomplete HJ population. Bonomo et al. (2017) found that a large sample of HJ parameters appeared to be shaped by host star tides. A complete population of HJs could enable follow-up investigations of these and other tentative trends and connect them to the physics of planet formation and evolution.

In this article, we present nine new HJs discovered by TESS, eight of which orbit an FGK star brighter than $G = 12.5$ mag. These planets were first detected via transit photometry by TESS and classified as TESS Objects of Interest (TOIs) before being confirmed by ground-based photometry, RVs, and high-resolution imaging (HRI). In Section 2, we discuss these observations in detail. In Section 3, we discuss the use of Markov Chain Monte Carlo to globally fit each planetary system and obtain relevant stellar and planetary parameters. In Section 4, we present the results of these global fits and discuss the future of our survey. Finally, in Section 5, we summarize the key arguments made in this article.

2. Observations

We used a combination of space-based and ground-based photometric, HRI, and spectroscopic observations to characterize each planetary system and rule out possible false-positive scenarios, such as eclipsing binaries, blended nearby eclipsing binaries, and stellar activity. Table 1 shows the relevant parameters of each system from archival observations and ground-based spectroscopy.

2.1. TESS Photometry

All nine of the planets confirmed in this work were first classified as candidates after transits were detected by TESS. The TESS spacecraft observes $24° \times 96°$ sectors of the sky for 27 days at a time, with a pixel scale of $21''$ pixel^{-1}. During TESS's Prime Mission (Sectors $1-26$), more than 200,000 bright stars were selected for 2-minute-cadence, high-precision photometry, while the remainder of the stars in the fields were observed in the 30-minute-cadence full-frame images. In TESS's first extended mission (Sectors $27-55$), 2-minute-cadence photometry was obtained for $\sim$15,000 stars per sector, and the cadence of the full-frame images was reduced to 10 minutes. In addition, approximately 600 targets per sector received 20 s cadence data. In the ongoing second extended mission (Sectors $56-97$), the full-frame images have 200 s

sampling, $\sim$8000 targets per sector will be selected for 2-minute cadence, and $\sim$2000 targets per sector will be selected for 20 s cadence.

The systems studied in this work were observed in at least two sectors each, between Sector 8 and Sector 63. These observations were collected in 2 minutes cadence, 10 minutes cadence, and 30 minutes cadence. The TESS data were reduced using both the TESS Science Processing Operations Center (SPOC) Pipeline (Jenkins et al. 2016; Caldwell et al. 2020; MAST 2021b; STScI 2022) located at NASA Ames Research Center and the MIT Quick-Look Pipeline (QLP; Huang et al. 2020a, 2020b; Huang 2020; Kunimoto et al. 2021). Both pipelines account for contamination from other stars in the pixel mask. Where available, the SPOC light curves were chosen over the QLP light curves. See Table 2 for a full list of the sectors and cadences in which each system was observed and the pipelines used to process the data. In the table, SPOC light curves generated from the full-frame images have their source listed as TESS-SPOC, as opposed to SPOC, which refers to the SPOC light curves from the 2 minutes data.

Both the SPOC and QLP pipelines search for and identify transit-like signals, which are then vetted by the TESS Science Office. The SPOC conducted its transit searches with an adaptive, noise-compensating matched filter (Jenkins et al. 2002, 2010, 2020), producing a threshold crossing event for which an initial limb-darkened transit model was fitted (Li et al. 2019) and a suite of diagnostic tests were conducted to help make or break the planetary nature of the signal (Twicken et al. 2018). Those that survive this process are identified as candidates, labeled TOIs (Guerrero et al. 2021), and are released to the public. The light curves were downloaded using the lightkurve[52] package (Lightkurve Collaboration et al. 1812), which accesses the Mikulski Archive for Space Telescopes (MAST[53]). The selected light curves were then flattened using keplersplinev2,[54] which fits a spline to any out-of-transit stellar variability in the light curve, which can then be divided out to flatten the light curve without significantly affecting the transit (Vanderburg & Johnson 2014). In order to optimally choose the spline break points, we adopted the methodology from Shallue & Vanderburg (2018) and used the choosekeplersplinev2 feature, which chooses the break-point spacing that minimizes the Bayesian information criterion (Schwarz 1978). We then chop the flattened light curves to ensure that only a baseline of one transit duration (T_{14}) is kept on either side of each transit to reduce the computational cost of using 27 day, nearly uninterrupted light curves in our global fits.

2.2. Ground-based Photometry

To confirm and better characterize each system, we collected ground-based photometric follow-up of all nine targets through the TESS Follow-up Observing Program (TFOP; Collins et al. 2018) Sub Group 1 (SG1; Collins 2019). This ground-based follow-up serves multiple purposes: to rule out contamination from nearby eclipsing binaries that were blended in TESS's larger pixels, to collect observations in multiple different bandpasses and rule out that the target star itself is an eclipsing binary, and to extend the observation baselines to provide

---

[52] https://github.com/lightkurve/lightkurve
[53] https://archive.stsci.edu/
[54] https://github.com/avanderburg/keplersplinev2

Table 1
Measured Properties from Literature

		TOI-1855	TOI-2107	TOI-2368	TOI-3321	TOI-3894	Source
Other identifiers:							
	TESS Input Catalog	TIC 81247740	TIC 446549906	TIC 401125028	TIC 306648160	TIC 165464482	
	TYCHO-2	TYC 1463-150-1	—	—	TYC 9062-2690-1	TYC 3850-280-1	
	2MASS	J13412503+1741141	J19071116−5841485	J08594984−4829182	J17430248−6500297	J13252998+5246050	
	Gaia DR3	1247603719345703808	6633448311454447232	5325498111172934784	5909085279371278336	1562935820172427392	
Astrometric parameters:							
$\alpha_{\rm J2000}$‡	R.A. (h:m:s)	13:41:25.028	19:07:11.162	08:59:49.838	17:43:02.481	13:25:29.974	1
$\delta_{\rm J2000}$‡	decl. (d:m:s)	17:41:13.99	−58:41:48.48	−48:29:18.269	−65:00:29.677	52:46:05.039	1
μ_α	Gaia DR3 proper motion in RA (mas yr^{-1})	−73.265 ± 0.017	3.703 ± 0.012	−5.084 ± 0.011	−0.048 ± 0.014	−8.895 ± 0.012	1
μ_δ	Gaia DR3 proper motion in Dec (mas yr^{-1})	−80.743 ± 0.011	−8.099 ± 0.011	−19.694 ± 0.01	−1.832 ± 0.016	8.650 ± 0.011	1
π	Gaia DR3 Parallax (mas)	5.6659 ± 0.0174	4.2151 ± 0.0146	4.7511 ± 0.0093	3.4852 ± 0.0213	2.3814 ± 0.0114	1
$v \sin i_\star$	Projected rotational velocity (km s^{-1})	5.74 ± 0.15	9.85 ± 0.34	10.60 ± 0.19	5.19 ± 0.13	5.27 ± 0.17	2
Photometric parameters:							
G	Gaia G mag.	11.18 ± 0.02	11.86 ± 0.02	12.27 ± 0.02	11.10 ± 0.02	11.69 ± 0.02	1
$G_{\rm BP}$	Gaia $G_{\rm BP}$ mag.	11.58 ± 0.02	12.23 ± 0.02	12.74 ± 0.02	11.41 ± 0.02	11.96 ± 0.02	1
$G_{\rm RP}$	Gaia $G_{\rm RP}$ mag.	10.61 ± 0.02	11.32 ± 0.02	11.64 ± 0.02	10.61 ± 0.02	11.26 ± 0.02	1
T	TESS mag.	10.650 ± 0.007	11.382 ± 0.006	11.696 ± 0.006	10.665 ± 0.006	11.323 ± 0.007	3
J	2MASS J mag.	9.979 ± 0.022	10.737 ± 0.026	10.916 ± 0.021	10.046 ± 0.021	10.78 ± 0.021	4
H	2MASS H mag.	9.620 ± 0.023	10.435 ± 0.026	10.509 ± 0.024	9.718 ± 0.021	10.51 ± 0.02	4
K	2MASS K mag.	9.523 ± 0.020	10.328 ± 0.021	10.342 ± 0.020	9.670 ± 0.021	10.479 ± 0.020	4
W1	WISE W1 mag.	9.354 ± 0.030	10.269 ± 0.031	10.355 ± 0.030	9.616 ± 0.030	10.447 ± 0.030	5
W2	WISE W2 mag.	9.404 ± 0.030	10.302 ± 0.031	10.445 ± 0.030	9.640 ± 0.030	10.487 ± 0.030	5
W3	WISE W3 mag.	9.376 ± 0.036	10.293 ± 0.075	10.364 ± 0.069	9.588 ± 0.040	10.449 ± 0.059	5

		TOI-3919	TOI-4153	TOI-5232	TOI-5301	Source
Other identifiers:						
	TESS Input Catalog	TIC 23769326	TIC 470171739	TIC 69356857	TIC 58825110	
	TYCHO-2	—	TYC 4612-244-1	—	—	
	2MASS	J13554673+4023304	J22213433+8212578	J19372100+3516360	—	
	Gaia DR3	1497132660589966976	2299246592282070400	2048174967505679488	2776823148593566592	
Astrometric parameters:						
$\alpha_{\rm J2000}$‡	R.A. (h:m:s)	13:55:46.738	22:21:34.307	19:37:21.0	00:51:57.604	1
$\delta_{\rm J2000}$‡	decl. (d:m:s)	40:23:30.487	82:12:57.759	35:16:35.933	13:04:41.835	1
μ_α	Gaia DR3 proper motion in RA (mas yr^{-1})	2.236 ± 0.010	16.409 ± 0.015	−14.071 ± 0.010	5.273 ± 0.259	1
μ_δ	Gaia DR3 proper motion in Dec (mas yr^{-1})	1.004 ± 0.011	8.158 ± 0.013	−35.962 ± 0.011	−5.756 ± 0.314	1
π	Gaia DR3 Parallax (mas)	1.6301 ± 0.0120	2.3424 ± 0.0109	1.6203 ± 0.0099	0.8934 ± 0.1932	1
$v \sin i_\star$	Projected rotational velocity (km s^{-1})	7.73 ± 0.09	9.44 ± 0.22	9.39 ± 0.23	11.80 ± 0.19	2
Photometric parameters:						
G	Gaia G mag.	12.70 ± 0.02	11.56 ± 0.02	12.16 ± 0.02	11.57 ± 0.02	1
$G_{\rm BP}$	Gaia $G_{\rm BP}$ mag.	12.98 ± 0.02	11.87 ± 0.02	12.44 ± 0.02	11.84 ± 0.02	1
$G_{\rm RP}$	Gaia $G_{\rm RP}$ mag.	12.27 ± 0.02	11.08 ± 0.02	11.71 ± 0.02	11.12 ± 0.02	1
T	TESS mag.	12.334 ± 0.007	11.148 ± 0.006	11.779 ± 0.009	11.189 ± 0.007	3
J	2MASS J mag.	11.819 ± 0.022	10.559 ± 0.023	11.182 ± 0.022	10.616 ± 0.023	4
H	2MASS H mag.	11.545 ± 0.020	10.359 ± 0.031	10.906 ± 0.021	10.405 ± 0.021	4
K	2MASS K mag.	11.502 ± 0.020	10.296 ± 0.021	10.857 ± 0.020	10.336 ± 0.020	4

Table 1
(Continued)

		TOI-3919	TOI-4153	TOI-5232	TOI-5301	Source
W1	WISE W1 mag.	11.476 ± 0.030	10.228 ± 0.030	10.804 ± 0.030	10.288 ± 0.030	5
W2	WISE W2 mag.	11.510 ± 0.030	10.234 ± 0.030	10.830 ± 0.030	10.298 ± 0.030	5
W3	WISE W3 mag.	11.507 ± 0.158	10.182 ± 0.054	10.753 ± 0.084	10.349 ± 0.094	5

Notes. The uncertainties of the photometric measurements have a systematic floor applied that is usually larger than the reported catalog errors.

[a] R.A. and decl. are in epoch J2000. The coordinates come from Vizier where the Gaia R.A. and decl. have been precessed and corrected to J2000 from epoch J2016.

References. (1) Gaia Collaboration et al. 2021; (2) Sections 2.3.1 and 2.3.2; (3) Stassun et al. 2019; (4) Cutri et al. 2003; Skrutskie et al. 2006; (5) Wright et al. 2010; Cutri et al. 2012.

Table 2
Summary of Observations from TESS

Target	TESS Sector	Cadence (s)	Source
TOI-1855	23	1800	TESS-SPOC
	50	120	SPOC
TOI-2107	13	1800	QLP
	27	600	QLP
TOI-2368	8	1800	TESS-SPOC
	9	1800	TESS-SPOC
	35	600	TESS-SPOC
	36	600	TESS-SPOC
	62	120	SPOC
	63	120	SPOC
TOI-3321	12	1800	TESS-SPOC
	13	1800	TESS-SPOC
TOI-3894	15	1800	TESS-SPOC
	16	1800	TESS-SPOC
	22	1800	TESS-SPOC
	49	120	SPOC
TOI-3919	16	1800	TESS-SPOC
	23	1800	TESS-SPOC
	49	120	SPOC
	50	120	SPOC
TOI-4153	18	1800	TESS-SPOC
	19	1800	TESS-SPOC
	24	1800	TESS-SPOC
	25	1800	TESS-SPOC
	26	1800	TESS-SPOC
	53	120	SPOC
	58	120	SPOC
	59	120	SPOC
	60	120	SPOC
TOI-5232	14	1800	QLP
	40	600	QLP
	41	600	QLP
	54	600	QLP
	55	600	QLP
TOI-5301	17	1800	TESS-SPOC
	42	600	TESS-SPOC
	43	600	TESS-SPOC

better constraints on the orbital period and transit epoch. The follow-up photometry from SG1 is included in our global analysis (see Section 3) and shown in Table 3. Additionally, for more detailed information on the follow-up observations collected for each of these planets, see Table 3. All 40 follow-up light curves are available to the public and can be downloaded from ExoFOP.[55]

The Las Cumbres Observatory Global Telescope (LCOGT; Brown et al. 2013) generated 12 of the follow-up light curves of our targets using observations from the following LCOGT sites: the Cerro Tololo Inter-American Observatory (CTIO), the Siding Spring Observatory (SSO), the South African Astronomical Observatory (SAAO), and the McDonald Observatory (McD). Additional ground-based observations of our targets were collected using the following facilities: the National Astronomical Observatory of Japan (NAOJ; Narita et al. 2015), Teide Observatory, Deep Sky West, the Southern Astrophysical Research (SOAR) telescope at CTIO, TRAPPIST-South at the La Silla Observatory (Jehin et al. 2011), El Sauce Observatory, Hazelwood Observatory, Brierfield Observatory,

KeplerCam at the Fred Lawrence Whipple Observatory (FLWO), the Acton Sky Portal, Observatori de Ca l'Ou (CALOU), Waffellow Creek Observatory (WCO), the Michigan State University (MSU) Observatory, Carlson R. Chambliss Astronomical Observatory (CRCAO) at Kutztown University, and the University of Louisville Manner Telescope (ULMT) at Mount Lemmon Observatory.

The data calibration and reduction for each follow-up observation (with the exception of the observations from MuSCAT and MuSCAT2; see Section 2.2.1) were done using AstroImageJ (AIJ; Collins et al. 2017), a tool designed to enable point-and-click photometry and data reduction. The exposures from the observation are first calibrated using flat-field images, dark images, and bias images by the observer or facility that collected the observations. The general procedure[56] that is then used to generate a reduced light curve for each target is as follows:

1. Generate calibrated images using AIJ's CCD Data Processor tool, median-combining the biases, darks, and flats, before subtracting the master bias and dark and dividing the master flat.
2. Locate the target star in the first image and develop an aperture that has a diameter of roughly twice the FWHM of the target. The background annulus should have roughly the same area as the target aperture.
3. Place apertures on the target star and at least 5–10 comparison stars of similar brightness. The number of comparison stars varies significantly depending on the field of view (FOV) of the telescope and the density of stars in the surrounding area of the sky.
4. Run AIJ's multiaperture photometry, which populates AIJ's measurement table and plot.
5. Assess the quality of the data and search for relevant parameters that change significantly throughout the observation and correlate with changes in the relative flux of the host star. Likely culprits usually include the air mass, the target star's X and Y pixel location (due to imperfect guiding), and the width or FWHM of the target source (due to evolving weather conditions).
6. Use AIJ's built-in transit-fitting tool to fit the transit with detrending enabled. Choose the detrending parameters from the previous step that minimize the Bayesian information criterion.
7. Normalize the relative flux and save a light curve file containing the Barycentric Julian Date in Barycentric Dynamical Time (BJD$_{TDB}$), normalized relative flux, relative flux error, and the selected detrending parameters.

This reduced light curve is then ready to be included in our global fit (see Section 3).

2.2.1. MuSCAT and MuSCAT2 Observations of TOI-1855

Two of the follow-up light curves that we obtained for TOI-1855 b were reduced using a reduction strategy different from the one presented above.

We observed TOI-1855 b using MuSCAT, a simultaneous multiband photometer installed on the 188 cm telescope of NAOJ in Okayama, Japan (Narita et al. 2015). It has three 1k

---

[56] For more details and observing tips, see Dennis Conti's guide: https://astrodennis.com/Guide.pdf.

Table 3
Follow-up Observations

TIC ID	TOI	Telescope	Camera	Observation Date (UT)	Telescope Size (m)	Filter	Pixel Scale (arcsec)	Exposure Time (s)	Detrending Parameters
81247740	1855	Astrosberge (Bergeron)	SBIG ST10xme	2020 May 13	0.305	Rc	1.85	38	Air mass, tot_C_cnts
		NAOJ-Okayama	MuSCAT	2021 Apr 5	1.88	g'	0.358	8	Air mass
		NAOJ-Okayama	MuSCAT	2021 Apr 5	1.88	r'	0.358	6	Air mass
		NAOJ-Okayama	MuSCAT	2021 Apr 5	1.88	z'	0.358	9	Air mass
		TCS	MuSCAT2	2020 May 19	1.52	g'	0.44	8	Air mass
		TCS	MuSCAT2	2020 May 19	1.52	r'	0.44	6	Air mass
		TCS	MuSCAT2	2020 May 19	1.52	i'	0.44	12–15[a]	Air mass
		TCS	MuSCAT2	2020 May 19	1.52	z'	0.44	9–12[a]	Air mass
		Deep Sky West	Apogee Ultra 16 m	2020 May 21	0.5	g'	1.09	90	BJD_TDB, FWHM_T1, air mass
		LCO-CTIO	Sinistro	2021 Jan 27	1	z'	0.39	40	Air mass
		SOAR	Goodman	2022 Apr 20	4.1	i'	0.15	25	Air mass, Y(FITS)_T1
446549906	2107	LCO-SSO	SBIG STX6303	2020 May 6	0.4	i'	0.57	300	Width_T1, Y(FITS)_T1
		LCO-SAAO	SINISTRO	2020 Jul 16	1	z'	0.389	70	Air mass
		LCO-SAAO	SINISTRO	2020 Jul 16	1	g'	0.389	26	Air mass
		TRAPPIST-South	FLI ProLine PL3041-BB	2023 May 10	0.6	B	0.64	50	None
401125028	2368	CDK14 (El Sauce)	STT-1603	2020 Nov 14	0.36	Rc	1.47	120	Air mass
		Hazelwood Observatory	STT3200	2021 Jan 20	0.32	Rc	0.556	180	Air mass
		LCO-SSO	Sinistro	2021 February 20	1	g'	0.39	47	Air mass
		LCO-SSO	Sinistro	2021 Feb 20	1	i'	0.39	27	Air mass
		SOAR	Goodman	2022 Apr 20	4.1	i'	0.15	40	Air mass
		LCO-CTIO	SINISTRO	2023 Apr 12	1	i'	0.389	27	Air mass
		LCO-CTIO	SINISTRO	2023 Apr 12	1	i'	0.389	40	Air mass
306648160	3321	LCO-SAAO	Sinistro	2022 Apr 30	1	z'	0.389	44	None
165464482	3894	KeplerCam	KeplerCam	2022 Jan 26	1.2	i'	0.672	10	Air mass
		KeplerCam	KeplerCam	2022 Mar 19	1.2	B	0.672	20	Air mass, X(FITS)_T1
		Acton Sky Portal	SBIG A4710	2023 Apr 09	0.36	r'	1	20	Air mass
23769326	3919	CALOU	FLI PL1001	2022 Jan 14	0.4	R	1.11	120	Air mass
		WCO	SBIG STXL-6303E	2022 Apr 28	0.36	r'	0.66	90	Meridian flip
		KeplerCam	KeplerCam	2022 Apr 28	1.2	i'	0.672	25	Air mass, X(FITS)_T1
		LCO-McD	Sinistro	2023 Mar 6	1	i'	0.389	46	Y(FITS)_T1
470171739	4153	MSU	Apogee Alta U47	2022 Jul3	0.6	V	0.55	60	Air mass
		MSU	Apogee Alta U47	2022 Aug 9	0.6	V	0.55	60	Air mass
		CRCAO-KU-OGS-RC	SBIG STXL-6303E	2022 Sep 16	0.61	B	0.76	120	Air mass, X(FITS)_T1
		CRCAO-KU-OGS-RC	SBIG STXL-6303E	2022 Sep 16	0.61	Ic	0.76	90	None
69356857	5232	ULMT	ASI 6200	2023 Jun 12	0.6	R	0.167	30	None
		LCO-McD	SINISTRO	2023 Jun 12	1	i'	0.389	27	Air mass
58825110	5301	KeplerCam	KeplerCam	2022 Oct 28	1.2	i'	0.672	7	Air mass

Notes. All light curves are available on ExoFOP.
[a] Exposure times were adjusted to avoid target saturation. Section 2.2.1 provides further details.

CCDs each with $6'.1 \times 6'.1$ FOV and $0''.358$ pixel^{-1} pixel scale, enabling simultaneous photometry in the g (400–550 nm), r (550–700 nm), and z_s (820–920 nm) bands. The data reduction and differential photometry were performed using the pipeline described in Fukui et al. (2011). We optimized both the aperture radii and the set of comparison stars by minimizing the

Table 4
The First RV Measurement of Each System, per Instrument Used

Target	Spectrograph	BJD_{TDB}	RV (m s^{-1})	σ_{RV} (m s^{-1})
TOI-1855	CHIRON	2459281.82160	−34358.0	29.0
TOI-2107	CHIRON	2459320.88131	2413.0	44.0
TOI-2368	CHIRON	2459299.60262	16039.0	64.0
TOI-3321	CHIRON	2459375.74691	12710.0	28.0
TOI-3894	TRES	2459405.67847	231	52.6
	NEID	2459709.79500	8084.2	10.4
TOI-3919	TRES	2459622.02268	679	39.9
TOI-4153	TRES	2459421.95883	251	48.5
TOI-5232	TRES	2459684.92784	409	53.2
TOI-5301	TRES	2459823.79933	−478	46.0

Note. The full table of RVs for each system is available in machine-readable form in the online journal.

dispersion of the resulting relative light curves. However, there are only two useful comparison stars within the FOV, one of which is a faint star 12″8 from the target. Using the brighter comparison star and uncontaminated aperture radius of 7″2 yielded the optimum light curves with a typical rms of 0.5 ppt/10 minutes across all bands.

We additionally observed TOI-1855 b with the 1.5 m Telescopio Carlos Sánchez (TCS) instrument MuSCAT2 (Narita et al. 2019) from Teide Observatory, Tenerife, Spain. MuSCAT2 is another multiband imager, equipped with four cameras with an FOV of 7.4 × 7.4 arcmin^2 (pixel scale of 0″44 pixel^{-1}) and is capable of obtaining simultaneous observations in g', r', i', and z_s bands. The exposure times were initially set to 8, 6, 15, and 12 s in g', r', i', and z_s, respectively. During the observations, the i'- and z_s-band exposure times were changed to 12 and 9 s, respectively, to avoid the saturation of the target star. The dedicated MuSCAT2 pipeline (Parviainen et al. 2019) reduced the raw science frames using standard procedures (i.e., dark and flat-field corrections) and computed the photometry for the stars in the field using a set of circular apertures. Finally, the pipeline obtained the best light curve by fitting a transit model that includes instrumental effect noise components and choosing the aperture that delivered the lowest scatter in the time series.

2.3. Spectroscopy

In order to rule out false-positive scenarios and measure the mass and orbital eccentricity of each planet, we collected spectroscopic observations of each host star to measure the RV shift imparted on the star by the orbiting planet. The spectra that we used in our final fits of the nine systems in this sample were collected by the Tillinghast Reflector Échelle Spectrograph (TRES) on the 1.5 m Tillinghast Reflector at FLWO (Fűrész 2008), the CHIRON spectrograph on the SMARTS 1.5 m telescope at CTIO (Tokovinin et al. 2013; Paredes et al. 2021), and the NEID spectrograph on the 3.5 m WIYN Telescope at the Kitt Peak National Observatory (KPNO; Schwab et al. 2016b). An example RV measurement is shown for each target and instrument in Table 4. Additionally, the spectroscopic metallicity measurements from TRES and CHIRON were averaged and used as a wide Gaussian prior in our EXOFASTv2 global fits, with a prior width equal to twice the standard deviation of the measured metallicities.

2.3.1. TRES Spectroscopy

Five of the nine host stars presented in this paper (TOI-3894, TOI-3919, TOI-4153, TOI-5232, and TOI-5301) were observed using TRES to obtain precise RVs. TRES is a fiber-fed, high-resolution échelle spectrograph mounted on a 1.5 m telescope with a resolving power (R) of 44,000. The reduction of the spectra was done following the work of Buchhave et al. (2010). Multiorder velocities were derived by cross-correlating the spectrum with the highest signal-to-noise ratio (SNR) per resolution element against each observation, order by order. To measure the metallicity, effective temperature, surface gravity, and projected rotational velocity of the star, we analyzed the spectra with the Stellar Parameter Classification (SPC) tool (Buchhave et al. 2012). Finally, we calculated the bisector spans of the TRES spectra following the work of Torres et al. (2007) to hunt for correlations between the bisector spans and RVs, an indication that the RVs are being induced by an eclipsing binary. For each of the five targets with TRES spectra, we found no evidence of correlation between the bisector spans and the RVs.

One of the secondary goals of our RV observations was to identify likely candidates for exterior planets by capturing the long-term RV trends of our target systems. In pursuit of this goal, we observed RV baselines of 354 days (UT 2021 July 10 −UT 2022 April 29) for TOI-3894, 132 days (UT 2022 February 11−UT 2022 June 23) for TOI-3919, 332 days (UT 2021 July 26−UT 2022 June 23) for TOI-4153, 82 days (UT 2022 April 15−UT 2022 July 6) for TOI-5232, and 69 days (UT 2022 September 1−UT 2022 November 9) for TOI-5301. A Lomb−Scargle periodogram was constructed for the RV residuals of each system that yielded no significant evidence of periodicity. However, of these systems, one has a potential long-term linear RV trend: TOI-3919. We identified a negative linear RV trend with a slope of $-0.79^{+0.31}_{-0.30}$ m s^{-1} day^{-1} over TOI-3919's 132-day baseline, following the prescription laid out in Section 3. Further follow-up observations of the TOI-3919 system could confirm the validity of the linear RV trend and identify the mass of an additional companion.

2.3.2. CHIRON Spectroscopy

The other four host stars in this work (TOI-1855, TOI-2107, TOI-2368, and TOI-3321) were observed using CHIRON, a fiber-fed, high-resolution échelle spectrograph. For the majority of the observations in this paper, we used an image slicer that offers a resolving power of ∼80,000. The exception to this is TOI-2107, of which we observed 23 spectra in the fiber mode ($R \sim 25,000$) before switching to the slicer mode for the remaining 13 observations. In both cases, we bracketed each of the spectra we collected with ThAr calibration spectra. To obtain estimates of the metallicity, effective temperature, surface gravity, and projected rotational velocity, each spectrum is matched to an interpolated catalog of ∼10,000 spectra classified by SPC (Buchhave et al. 2012). RVs were derived by the least-squares deconvolution (Donati et al. 1997; Zhou et al. 2021) of the observed spectra against nonrotating synthetic templates generated using ATLAS9 model atmospheres (Kurucz 1992), before fitting the resulting line profile with a rotational broadening kernel prescribed by Gray (2005).

Our CHIRON observations spanned baselines of 655 days (UT 2020 July 9−UT 2022 April 25) for TOI-1855, 501 days (UT 2021 April 16−UT 2022 August 30) for TOI-2107,

445 days (UT 2021 March 26−UT 2022 April 14) for TOI-2368, and 445 days (UT 2021 June 10−UT 2022 August 29) for TOI-3321. Of these systems, we found no evidence of additional periodicity, but again we found a tentative linear trend in TOI-2368's RVs with a slope of 0.21 ± 0.11 m s^{-1} day^{-1}. Further observations to extend the 445-day baseline could identify whether or not this signal is real and corresponds to a distant planetary or stellar companion.

2.3.3. NEID Spectroscopy

We obtained six observations of TOI-3894 with the NEID spectrograph, between UT 2022 April 29 and UT 2022 June 09. NEID is a highly stabilized, fiber-fed optical spectrograph (Halverson et al. 2016; Schwab et al. 2016) on the WIYN 3.5 m telescope at KPNO. We used NEID in high-resolution (HR) mode ($R \sim 110{,}000$), and the data were reduced using versions 1.1.2–1.1.4 of the NEID Data Reduction Pipeline (DRP). The DRP extracts precise RVs by cross-correlating the observed spectra with a stellar line mask (Baranne et al. 1996; Pepe et al. 2002). Each observation was made with exposure times between 300 and 420 s, achieving a typical RV precision of ≈ 10 m s^{-1}. On the nights of 2022 May 9 and 10, the NEID data were affected by a failure of the Fabry–Perot etalon laser, which is used to calibrate nightly offsets. We used observations of standard stars to determine those offsets (35.8 ± 1.2 m s^{-1} and 31.5 ± 1.3 m s^{-1}, respectively; see Yee et al. 2023) and correct the NEID RVs taken on the affected nights.

2.4. Supplementary Spectroscopy

Three additional spectra of TOI-1855 were collected by the Skalnaté Pleso Observatory in the High Tatras (Slovak Republic), using the 1.3 m f/8.36 Astelco Alt-azimuthal Nasmyth−Cassegrain reflecting telescope, equipped with a fiber-fed échelle spectrograph of MUSICOS design (Baudrand & Bohm 1992). The spectral range of the instrument is 4250–7375 Å (56 échelle orders) with a maximum resolving power of $R = 38{,}000$. The raw data were then reduced using IRAF package tasks, Linux shell scripts, and FORTRAN programs (Pych 2004; Pribulla et al. 2015; Garai et al. 2017).

Finally, seven spectra were collected using the Ondřejov Echelle Spectrograph (OES) installed at the 2 m Perek telescope at the Astronomical Institute of the Czech Academy of Sciences in Ondřejov, Czechia. OES provides a wavelength range of 3750–9200 Å and a spectral resolving power of 50,000. See Koubský et al. (2004) and Kabáth et al. (2020) for more details about OES. The data were reduced using standard IRAF procedures.

These RVs were used to increase our confidence that TOI-1855 b is a bona fide exoplanet. Because there were fewer observations from these telescopes with lower precision than the CHIRON data, we did not include them in our EXOFASTv2 global fit. However, these observations were consistent with the 204^{+16}_{-15} ms^{-1} RV semiamplitude measured by CHIRON.

2.5. High-resolution Imaging

Close stellar companions (bound or line of sight) can confound exoplanet discoveries in a number of ways. The detected transit signal might be a false positive due to a nearby eclipsing binary, and even real planet discoveries will yield incorrect stellar and exoplanet parameters if a close companion exists and is unaccounted for (Ciardi et al. 2015; Furlan & Howell 2017). Additionally, the presence of a close companion star leads to the nondetection of small planets residing in the same exoplanetary system (Lester et al. 2021). Given that nearly one-half of solar-like stars are in binary or multistar systems (Matson et al. 2018), HRI provides crucial information toward our understanding of exoplanet formation, dynamics, and evolution (Howell et al. 2021).

In order to understand and properly account for the light contribution of nearby field stars and stellar companions, we observed all nine of the host stars in our sample using adaptive optics (AO) and speckle imaging. Both of these techniques are capable of high angular resolution and allow us to place upper limits on the brightness of a nearby star and therefore the potential of any nearby star to contaminate the signal in the photometric and spectroscopic data.

Twenty AO and speckle observations from eight different instruments were used to find or rule out nearby contaminants to the host stars in this paper. The results of these observations are presented in the following sections, organized by the instrument used. Examples of a nondetection (TOI-3919) and positive detection (TOI-5232) of a nearby stellar companion are presented in Figure 1. The remainder of the high-resolution images and sensitivity curves are available on ExoFOP and are described in Sections 2.5.1 and 2.5.2 and presented in Table 5.

2.5.1. Adaptive Optics

Three AO instruments were employed to observe the stars studied in this work: the ShARCS camera on the Shane 3 m telescope at Lick Observatory (Kupke et al. 2012; Gavel et al. 2014; McGurk et al. 2014; Dressing et al., in preparation), the PHARO instrument on the Hale 5 m telescope at Palomar Observatory (Hayward et al. 2001), and the NIRC2 instrument on the Keck II 10 m telescope at Keck Observatory (Wizinowich et al. 2000).

The ShARCS observations of TOI-1855 were taken with the Shane AO system in natural guide star mode. We collected sequences of observations using a K_s filter ($\lambda_0 = 2.150$ μm, $\Delta\lambda = 0.320$ μm) and a J filter ($\lambda_0 = 1.238$ μm, $\Delta\lambda = 0.271$ μm). We reduced the data using the publicly available SImMER pipeline (Savel et al. 2020, 2022).[57] This observation ruled out any bright stellar companions other than TIC 81247738, the source with a separation of $12\rlap{.}''352$ already identified by Gaia.

Additionally, we observed TOI-1855, TOI-3894, and TOI-3919 with the PHARO instrument (Hayward et al. 2001) on the Palomar Hale (5 m) behind the P3K natural guide star AO system (Dekany et al. 2013) in the narrowband Brγ filter ($\lambda_0 = 2.1686$, $\Delta\lambda = 0.0326$ μm). The PHARO pixel scale is $0\rlap{.}''025$ pixel^{-1}. A standard five-point quincunx dither pattern with steps of $5''$ was repeated twice, with each repeat separated by $0\rlap{.}''5$. The final resolutions of the combined dithers were determined from the FWHM of the point-spread functions: $0\rlap{.}''09$.

Observations of TOI-5232 were made with the NIRC2 instrument behind the natural guide star AO system (Wizinowich et al. 2000) in the standard three-point dither pattern that is used with NIRC2 to avoid the lower left quadrant of the detector, which is typically noisier than the other three quadrants. The dither pattern step size was $3''$ and was repeated twice, with each dither
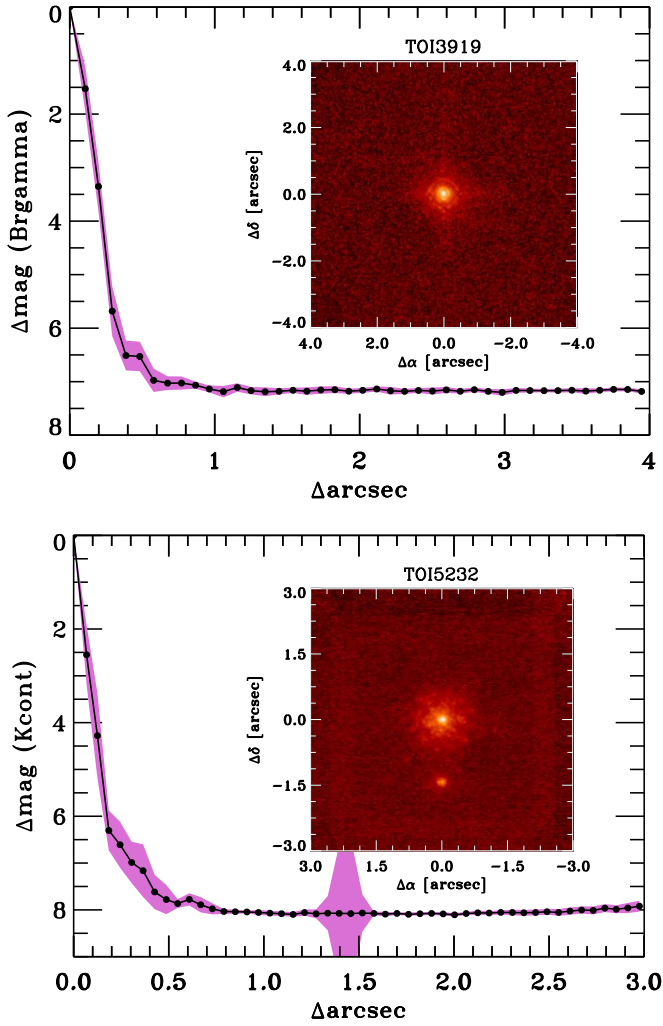
---

[57] https://github.com/arjunsavel/SImMER

Figure 1. AO images and sensitivity curves for TOI-3919 and TOI-5301. Top: Palomar PHARO AO image and 5σ sensitivity curve of TOI-3919 showing no detection of a companion star, down to the detection limits of the instrument. The magenta shaded region represents the uncertainty on the contrast curve. Bottom: Keck2 NIRC2 AO image and 5σ sensitivity curve of TOI-5232, showing a clear detection of a stellar companion at a separation of 1″417 with Δmag = 2.952 in the Kcont filter.

offset from the previous dither by 0″5. NIRC2 was used in the narrow-angle mode with a full FOV of $\sim10″$ and a pixel scale of approximately 0″0099442 pixel^{-1}. The NIRC2 observations were made in the Kcont filter ($\lambda_o = 2.2706$, $\Delta\lambda = 0.0296\,\mu$m) and the Hcont filter ($\lambda_o = 1.5804$, $\Delta\lambda = 0.0232\,\mu$m). The final resolutions of the combined dithers were once again determined from the FWHM of the point-spread functions: 0″067.

For both the PHARO and the NIRC2 images, the sensitivities of the final combined AO image were determined by injecting simulated sources azimuthally around the primary target every 20° at separations of integer multiples of the central source's FWHM (Furlan et al. 2017). The brightness of each injected source was scaled until standard aperture photometry detected it with 5σ significance. The final 5σ limit at each separation was determined from the average of all of the determined limits at that separation, and the uncertainty on the limit was set by the rms dispersion of the azimuthal slices at a given radial distance. Only TOI-5232 shows a close

companion—also detected in the optical speckle data (further described in Section 2.5.2) and by Gaia.

2.5.2. Speckle Imaging

In addition to our AO observations, five speckle instruments were used to observe the stars in our sample: the speckle polarimeter on the 2.5 m telescope at the Caucasian Mountain Observatory of the Sternberg Astronomical Institute (SAI) at Lomonosov Moscow State University, the HRCam instrument on the 4.1 m Southern Astrophysical Research (SOAR) telescope (Tokovinin 2018) at CTIO, the NN-EXPLORE Exoplanet Stellar Speckle Imager (NESSI; Scott et al. 2018) on the WIYN 3.5 m telescope at KPNO, and the Zorro and 'Alopeke instruments on the Gemini South and Gemini North 8 m telescopes, respectively (Scott et al. 2021).

The HRCam observations were made of TOI-1855, TOI-2107, TOI-2368, and TOI-3321 in the Cousins I band, a similar visible bandpass to that of TESS. The four observations were typically sensitive to a 5 mag fainter star at an angular distance of 1″ from the target. More details of the speckle observations from the SOAR TESS survey are available in Ziegler et al. (2020). A 4.6 mag fainter star was detected at a separation of 0″69 from TOI-3321. No nearby stars were detected within 3″ of TOI-1855, TOI-2107, or TOI-2368 in the SOAR observations.

TOI-1855, TOI-3919, TOI-4153, and TOI-5301 were observed with the SAI speckle polarimeter. The speckle polarimeter used an Electron Multiplying CCD (EMCCD) Andor iXon 897 as its main detector prior to 2022 August (Safonov et al. 2017). Since then, it has used the high-speed, low-noise CMOS detector Hamamatsu ORCA-Quest (Strakhov et al. 2023). The atmospheric dispersion compensator was active in all cases. Observations were carried out in the I_c band, where the respective angular resolution is 0″083. No nearby stars were detected in any of the SAI images.

The NN-EXPLORE Exoplanet Stellar Speckle Imager (Scott et al. 2018) was used to obtain speckle imaging of TOI-1855 and TOI-3894. NESSI is a dual-channel speckle imager at the WIYN 3.5 m telescope on Kitt Peak, Arizona. TOI-1855 was observed with two filters having central wavelengths of $\lambda_c = 562$ and 832 nm. It was then reobserved using only the 832 nm filter. TOI-3894 was observed using only the 832 nm filter. For each observation, the star was observed by taking nine sets of 1000 40 ms exposures in a 256×256 pixel section of the EMCCD for a 4″6 × 4″6 FOV centered on the target. A nearby single star was observed in close temporal proximity to each science target using a set of 1000 exposures to serve as a measure of the point-spread function. The speckle pipeline data reduction followed the description given in Howell et al. (2011). No companion sources were detected for either TOI-1855 or TOI-3894.

Finally, TOI-3321 and TOI-5232 were observed using the Zorro and 'Alopeke speckle instruments mounted on the Gemini South/North 8 m telescopes (Scott et al. 2021). Zorro and 'Alopeke both provide simultaneous speckle imaging in two bands (562 and 832 nm) with output data products including Fourier analysis and reconstructed images with robust contrast limits on companion detections. Seven sets of 1000×0.06 s images were obtained for TOI-3321, and 10 sets of 1000×0.06 s images were obtained for TOI-5232. Each of the observations was processed using our standard reduction

Table 5
Summary of High-resolution Imaging Observations

Target	Telescope	Instrument	Image Type	Filter	Contrast	Observation Date (UT)	Detection?[a]
TOI-1855	SAI (2.5 m)	Speckle polarimeter	Speckle	I_c	Δ6.2 mag at 1″	2020 Dec 29	No
	Palomar (5 m)	PHARO	AO	Brγ	Δ6.732 mag at 0″.5	2021 Feb 24	No
	SOAR (4.1 m)	HRCam	Speckle	I_c	Δ6.4 mag at 1″	2021 Feb 27	No
	Shane (3 m)	ShARCS	AO	K_s	—	2021 Mar 28	No
	Shane (3 m)	ShARCS	AO	J	—	2021 Mar 28	No
	WIYN (3.5 m)	NESSI	Speckle	562 nm	—	2021 Apr 1	No
	WIYN (3.5 m)	NESSI	Speckle	832 nm	—	2021 Apr 1	No
	WIYN (3.5 m)	NESSI	Speckle	832 nm	—	2021 Apr 18	No
TOI-2107	SOAR (4.1 m)	HRCam	Speckle	I_c	Δ6.0 mag at 1″	2021 Jul 14	No
TOI-2368	SOAR (4.1 m)	HRCam	Speckle	I_c	Δ5.8 mag at 1″	2020 Dec 29	No
TOI-3321	SOAR (4.1 m)	HRCam	Speckle	I_c	Δ7.0 mag at 1″	2021 Jul 14	Yes
	Gemini (8 m)	Zorro	Speckle	832 nm	Δ6.23 mag at 0″.5	2021 Jul 23	Yes
TOI-3894	WIYN (3.5 m)	NESSI	Speckle	832 nm	—	2022 Apr 17	No
	Palomar (5 m)	PHARO	AO	Brγ	Δ7.278 mag at 0″.5	2022 Jul 15	No
TOI-3919	Palomar (5 m)	PHARO	AO	Brγ	Δ6.529 mag at 0″.5	2022 Jul 15	No
	SAI (2.5 m)	Speckle polarimeter	Speckle	I_c	Δ5.1 mag at 1″	2023 Jan 19	No
TOI-4153	SAI (2.5 m)	Speckle polarimeter	Speckle	I_c	Δ4.9 mag at 1″	2021 Jul 19	No
TOI-5232	Keck2 (10 m)	NIRC2	AO	Hcont	Δ7.017 mag at 0″.5	2022 Nov 8	Yes
	Keck2 (10 m)	NIRC2	AO	Kcont	Δ7.779 mag at 0″.5	2022 Nov 8	Yes
	Gemini (8 m)	'Alopeke	Speckle	562 nm	Δ5.92 mag at 0.″5	2022 Nov 14	Yes
	Gemini(8 m)	'Alopeke	Speckle	832 nm	Δ7.0 mag at 0″.5	2022 Nov 14	Yes
TOI-5301	SAI (2.5 m)	Speckle polarimeter	Speckle	I_c	Δ6.1 mag at 1″	2022 Nov 18	No

Note. All images and contrast curves are available on ExoFOP.
[a] Detection refers to a positive detection of a star within the FOV of the AO or speckle instrument, subject to the maximum contrast possible with the instrument in question. TOI-1855's companion was outside of the FOV of each instrument that observed it.
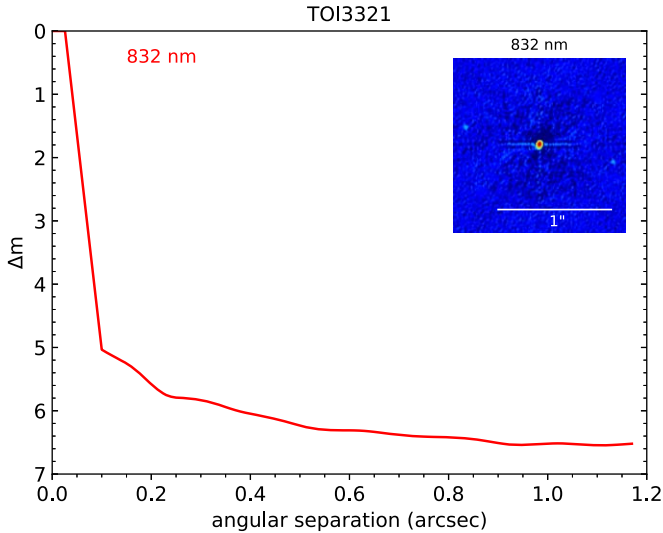
Figure 2. Speckle high-resolution image and 5σ sensitivity curve from Gemini's Zorro speckle imager. The observation reveals a source 79°.1 east of north and 0″.663 away from TOI-3321 that is 4.89 mag fainter in Zorro's 832 nm narrowband filter.

pipeline (see Howell et al. 2011). Figure 2 shows our final 5σ contrast curve and the reconstructed speckle image from the TOI-3321 observation. We find that TOI-3321 has a close companion with a separation of 0″.663 at a position angle of 79°.1 and is only detected in the 832 nm filter. The delta magnitude in the 832 nm filter, which is the magnitude of the companion relative to the primary star at 832 nm, is 4.89 mag. TOI-5232 also reveals a companion star at a separation of 1″.23

and position angle of 5°.2. This companion was detected in both filters and has delta magnitudes of 5.10 ± 0.5 (562 nm) and 4.64 ± 0.48 (832 nm), with both delta magnitude values being fairly uncertain owing to the large separation ($>1″.0$) for which the speckles are decorrelated. At the distance of TOI-3321 ($d = 286$ pc) and TOI-5232 ($d = 609$ pc) the angular limits from the diffraction limit (20 mas) out to 1″.2 correspond to spatial limits of 5.7–343 au and 12–727 au respectively.

2.5.3. Possible Stellar Companions

Of the nine planet-hosting stars in our sample, three (TOI-1855, TOI-3321, and TOI-5232) have nearby stars that are likely associated with our targets. The likely companions of TOI-1855 and TOI-5232 were both observed by Gaia and have distances and proper motions that are consistent with their probable host stars. TOI-3321's nearby star is faint, with Δmag ∼ 4.6−4.9, and is fairly close to TOI-3321, with a separation of ∼0″.679. This source doesn't appear to be associated with any of the nearby Gaia DR3 (Gaia Collaboration et al. 2023) detections. The Gaia Renormalized Unit Weight Error (RUWE), a metric that is used to determine whether or not the astrometric solution of a star is well-behaved for a single source, of this target is 1.283, which is less than the upper threshold of RUWE = 1.4, indicating that the Gaia solution is a well-behaved solution for a single source. A speckle image of TOI-3321 and the corresponding sensitivity curve from Gemini's Zorro speckle imager are shown in Figure 2, illustrating the detection of TOI-3321's faint companion.

TOI-1855 and its tentative stellar companion have a Δmag of 1.94 in the Brγ filter, which is small enough to influence TOI-1855's light curve; however, the $12''.352$ separation is distant enough that the Bergeron, MuSCAT, MuSCAT2, LCO-CTIO, and SOAR observations were all able to separate the stars and create uncontaminated light curves, confirming that the transit signal is not the consequence of a blended eclipsing binary. Additionally, the companion is distant enough that the spectral energy distribution (SED) of TOI-1855 (see Figure 6) is unaffected by the light from the companion. TOI-3321's tentative stellar companion is fainter than TOI-3321 by 4.89 mag in Gemini's 832 nm filter, which is too faint to significantly influence our light curve. Similarly, TOI-5232's tentative stellar companion is fainter than TOI-5232 by 4.64 mag in the same filter and is also too faint to significantly influence the photometry.

2.6. Archival Multiband Observations

In order to constrain the SED of the stars in our sample, we queried Vizier (Ochsenbein et al. 2000) to obtain broadband observations from Gaia EDR3 (Gaia Collaboration et al. 2021), the Two Micron All Sky Survey (2MASS; Cutri et al. 2003; Skrutskie et al. 2006), and the Wide-field Infrared Survey Explorer (WISE; Wright et al. 2010; Cutri et al. 2012). All of our targets were observed in the Gaia G, $G_{\rm BP}$, and $G_{\rm RP}$; 2MASS J, H, and K_s; and WISE W1, W2, and W3 bandpasses, which provide wavelength coverage from $\sim$0.3 to 12 μm. In addition, astrometric measurements from Gaia EDR3 were obtained in order to place a Bayesian prior on the parallax of each target (see Section 3.1 for more details). These archival observations were then used in our EXOFASTv2 global fits to determine relevant stellar parameters (see Section 3). These photometric and astrometric parameters are reported in Table 1.

3. Exofastv2 Global Fits

We used the publicly available code EXOFASTv2[58] (Eastman et al. 2019) to determine all of the system parameters for all nine of the targets in this work. EXOFASTv2 is a differential evolution Markov Chain Monte Carlo (MCMC) code, written in IDL, designed to globally fit both the star(s) and planet(s) in each system together, ensuring a self-consistent set of parameters describing each system. These fits combine the TESS data (discussed in Section 2.1), follow-up transit observations from the ground (discussed in Section 2.2), and the archival multiband photometric observations (discussed in Section 2.6) to generate an SED model using MESA Isochrones and Stellar Tracks (MIST; Paxton et al. 2011, 2013) and a transit model simultaneously at each step of the MCMC. Additional details about the EXOFASTv2 modeling suite can be found in Eastman et al. (2019).

To test for long-term RV trends, we ran an initial fit for each system, allowing for a linear trend in the RVs. If the fit found that the slope of this trend was more than 1σ away from zero, we fit for the linear trend in the final fit; otherwise, the slope was fixed at zero. There were only two cases in which a tentative long-term RV trend was found: TOI-2368 and TOI-3919. In all of the fits, we allowed the planet's orbital eccentricity to be a free parameter. In doing this, we provide a

measurement and estimated uncertainty for the orbital eccentricity of each of the systems in this study, as other derived parameters depend on eccentricity. However, because of the Lucy−Sweeney bias (Lucy & Sweeney 1971), eccentricities that are smaller than 2.45σ above zero should be considered consistent with a circular orbit (Eastman et al. 2019).

The resulting median and 68% confidence interval of all relevant planetary and stellar parameters for each system are presented in Table 6. Two of the systems that we fit had bimodal posterior distributions in stellar mass and age. These systems are discussed in further detail in Section 4.2.

3.1. Priors and Constraints

In all nine fits, we adopted Gaussian priors for the Gaia parallax measurements from Early Data Release 3 (Gaia Collaboration et al. 2021). We also placed wide Gaussian priors on the stellar metallicity, using averaged metallicity measurements from the TRES and CHIRON spectra, with a prior width equal to twice the standard deviation of the spectroscopic metallicities. Finally, we account for the possible contamination of the TESS target pixel by fitting a dilution term and placing a Gaussian prior centered at 0% with a standard deviation that is 10% of the dilution factor from the TESS Input Catalog (TIC) v8.2 (Stassun et al. 2018, 2019). This contamination is already corrected by both the QLP and SPOC pipelines (see Section 2.1), so this prior acts as a conservative assumption that the contamination correction had a precision better than 10%. Finally, we placed an upper limit on the V-band extinction of each target using the Schlegel et al. (1998) and Schlafly & Finkbeiner (2011) dust maps. Each of these priors is included at the top of Table 6.

In addition to the supplied Gaussian priors, we adopt starting values for the stellar mass, stellar radius, and stellar effective temperature from the TIC. To provide a constraint on the stellar radius, we apply an upper limit on the V-band extinction from Schlafly & Finkbeiner (2011). Finally, the starting values for the transit epoch T_C, orbital period P, and ratio of planetary and stellar radii R_P/R_* for our initial fit are retrieved from the TESS mission catalog on ExoFOP.[59]

One of our targets, TOI-1855, has a grazing transit configuration, in which the planet incompletely transits the limb of the star. As a result, the radius of this planet is poorly constrained. To account for the effectively flat radius posterior and to reduce the computational cost of the fit, we placed a generous physical upper limit on the radius of the planet, equal to $2.5R_J$. This upper limit is significantly larger than the largest nongrazing, transiting planet (Smalley et al. 2012), ensuring that our interpretation is not affected by the placement of a strict upper limit. The upper limit does, however, likely affect the median of the R_P posterior listed in Table 6, and so, for that reason, we also highlight the posterior mode, $1.38R_J$, as the most likely radius of the planet, illustrated with a vertical dashed line in Figure 3. A more detailed discussion of TOI-1855 and our interpretation of the radius distribution is included in Section 4.1.

4. Results and Discussion

In this first installment of the MEEP survey, we confirm nine new HJs (TOI-1855 b, TOI-2107 b, TOI-2368 b, TOI-3321 b,

---

Table 6
Median Values and 68% Confidence Intervals for Fitted Stellar and Planetary Parameters

		TOI-1855	TOI-2107	TOI-2368	TOI-3321	TOI-3894
Priors:						
π	Gaia parallax (mas)	$\mathcal{G}[5.6565, 0.04552]$	$\mathcal{G}[4.2477, 0.034]$	$\mathcal{G}[4.7622, 0.0262]$	$\mathcal{G}[3.5126, 0.0398]$	$\mathcal{G}[2.4301, 0.0227]$
[Fe/H]	Metallicity (dex)	$\mathcal{G}[0.4055, 0.085]$	$\mathcal{G}[0.0492, 0.1384]$	$\mathcal{G}[0.0461, 0.2318]$	$\mathcal{G}[-0.3127, 0.1593]$	$\mathcal{G}[-0.1229, 0.1743]$
A_V	V-band extinction (mag)	$\mathcal{U}[0, 0.05518]$	$\mathcal{U}[0, 0.15159]$	$\mathcal{U}[0, 5.7474]$	$\mathcal{U}[0, 0.20491]$	$\mathcal{U}[0, 0.03782]$
D_T	Dilution in TESS	$\mathcal{G}[0, 0.0060132]$	$\mathcal{G}[0, 0.081363]$	$\mathcal{G}[0, 0.006256]$	$\mathcal{G}[0, 0.00477]$	$\mathcal{G}[0, 0.000040424]$
Stellar parameters:						
M_*	Mass ($M_\odot$)	$0.987^{+0.057}_{-0.046}$	$0.961^{+0.049}_{-0.054}$	$0.897^{+0.048}_{-0.049}$	$1.041^{+0.084}_{-0.068}$	$1.138^{+0.089}_{-0.075}$
R_*	Radius ($R_\odot$)	$1.041^{+0.031}_{-0.033}$	$0.932^{+0.027}_{-0.024}$	$0.846^{+0.031}_{-0.026}$	$1.549^{+0.067}_{-0.062}$	$1.502^{+0.055}_{-0.052}$
L_*	Luminosity ($L_\odot$)	$0.804^{+0.031}_{-0.03}$	$0.786^{+0.035}_{-0.036}$	$0.531^{+0.1}_{-0.065}$	$2.54^{+0.15}_{-0.16}$	$2.624^{+0.092}_{-0.083}$
ρ_*	Density (cgs)	$1.23^{+0.15}_{-0.11}$	$1.68^{+0.12}_{-0.16}$	$2.1^{+0.19}_{-0.23}$	$0.396^{+0.07}_{-0.059}$	$0.475^{+0.065}_{-0.059}$
$\log g$	Surface gravity (cgs)	$4.397^{+0.04}_{-0.031}$	$4.484^{+0.024}_{-0.024}$	$4.538^{+0.027}_{-0.038}$	$4.076^{+0.057}_{-0.053}$	$4.143^{+0.043}_{-0.046}$
$T_{\rm eff}$	Effective temperature (K)	5359^{+89}_{-83}	5627^{+94}_{-93}	5360^{+230}_{-170}	5850 ± 140	6000 ± 110
[Fe/H]	Metallicity (dex)	$0.399^{+0.069}_{-0.078}$	$0.07^{+0.12}_{-0.11}$	$0.1^{+0.18}_{-0.15}$	$-0.103^{+0.047}_{-0.062}$	$0.021^{+0.085}_{-0.06}$
[Fe/H]$_0^\ddagger$	Initial metallicity	$0.389^{+0.064}_{-0.073}$	0.06 ± 0.11	$0.09^{+0.17}_{-0.15}$	$-0.026^{+0.054}_{-0.067}$	$0.096^{+0.073}_{-0.059}$
Age	Age (Gyr)	$8.1^{+3.5}_{-4}$	$4.0^{+4}_{-2.7}$	$4.2^{+5.1}_{-3}$	8.1 ± 2.4	$5.7^{+2.3}_{-1.8}$
EEP	Equivalent evolutionary phase	393^{+20}_{-43}	343^{+32}_{-31}	337^{+28}_{-37}	$447.2^{+8.3}_{-16}$	427^{+18}_{-30}
A_V	V-band extinction (mag)	$0.03^{+0.018}_{-0.02}$	$0.095^{+0.04}_{-0.056}$	$0.34^{+0.23}_{-0.2}$	$0.147^{+0.042}_{-0.073}$	$0.02^{+0.012}_{-0.013}$
d	Distance (pc)	176.8 ± 1.4	$235.4^{+1.9}_{-1.8}$	210.0 ± 1.2	$284.8^{+3.3}_{-3.2}$	$411.9^{+3.9}_{-3.8}$
Planetary parameters:						
P	Period (days)	1.36414864 ± 0.0000005	2.4545467 ± 0.0000013	5.1750073 ± 0.0000016	$3.6525145^{+0.0000027}_{-0.0000028}$	4.3345401 ± 0.0000022
R_P	Radius (R_J)	$1.64^{+0.52}_{-0.37}$	$1.211^{+0.035}_{-0.032}$	$0.967^{+0.036}_{-0.064}$	$1.388^{+0.07}_{-0.064}$	$1.358^{+0.054}_{-0.052}$
M_P	Mass (M_J)	$1.135^{+0.095}_{-0.094}$	0.83 ± 0.11	0.65 ± 0.18	$0.554^{+0.076}_{-0.075}$	0.85 ± 0.15
T_C	Time of conjunction (BJD$_{\rm TDB}$)	$2458929.44325^{+0.00031}_{-0.00032}$	$2458654.61784^{+0.0004}_{-0.00039}$	$2459297.19485^{+0.00026}_{-0.00028}$	$2458681.48898^{+0.00044}_{-0.00041}$	$2458912.41363^{+0.00041}_{-0.00042}$
T_0	Optimal conjunction time (BJD$_{\rm TDB}$)	$2459243.19743 \pm 0.00029$	$2459228.98176 \pm 0.00024$	$2459752.59549^{+0.00022}_{-0.00023}$	$2458940.81751^{+0.00039}_{-0.00036}$	$2459250.50775^{+0.00036}_{-0.00038}$
a	Semimajor axis (au)	$0.02398^{+0.00046}_{-0.00037}$	$0.03515^{+0.00059}_{-0.00067}$	0.05649 ± 0.001	$0.047^{+0.0012}_{-0.001}$	$0.0543^{+0.0014}_{-0.0012}$
i	Inclination (deg)	$78.12^{+0.99}_{-1}$	$89.44^{+0.39}_{-0.58}$	$86.61^{+0.39}_{-0.29}$	$86.33^{+1.3}_{-0.95}$	$84.86^{+0.43}_{-0.48}$
e	Eccentricity	$0.033^{+0.038}_{-0.023}$	$0.033^{+0.038}_{-0.023}$	$0.061^{+0.066}_{-0.042}$	$0.054^{+0.057}_{-0.038}$	$0.048^{+0.052}_{-0.034}$
ω_*	Argument of periastron (deg)	-100.0^{+120}_{-110}	153.0^{+100}_{-97}	121.0^{+63}_{-91}	12.0^{+98}_{-100}	-190.0^{+110}_{-100}
$T_{\rm eq}$	Equilibrium temperature (K)	1701.0 ± 20	1397.0^{+20}_{-18}	1000.0^{+44}_{-31}	1616.0^{+29}_{-28}	1519.0^{+22}_{-21}
$\tau_{\rm circ}$	Tidal circularization timescale (Gyr)	$0.00106^{+0.0028}_{-0.00079}$	$0.0452^{+0.024}_{-0.0094}$	$2.43^{+0.89}_{-0.89}$	$0.085^{+0.032}_{-0.024}$	$0.332^{+0.1}_{-0.088}$
K	RV semiamplitude (m s^{-1})	204^{+16}_{-15}	128^{+17}_{-16}	81 ± 23	$71.2^{+9.1}_{-9.2}$	96 ± 16
R_P/R_*	Radius of planet in stellar radii	$0.162^{+0.05}_{-0.035}$	$0.1335^{+0.0012}_{-0.0011}$	$0.11742^{+0.00069}_{-0.0007}$	0.0921 ± 0.0015	$0.0929^{+0.00078}_{-0.0008}$
a/R_*	Semimajor axis in stellar radii	$4.95^{+0.2}_{-0.15}$	$8.13^{+0.2}_{-0.27}$	$14.37^{+0.42}_{-0.42}$	$6.54^{+0.36}_{-0.34}$	7.79 ± 0.34
Depth	TESS flux decrement at midtransit	$0.00707^{+0.00028}_{-0.0003}$	$0.02131^{+0.00054}_{-0.00053}$	0.01283 ± 0.00011	$0.00966^{+0.00029}_{-0.00028}$	$0.008974^{+0.000089}_{-0.000091}$
τ	Ingress/egress transit duration (days)	$0.02489^{+0.00025}_{-0.00027}$	$0.01288^{+0.00029}_{-0.00017}$	$0.02452^{+0.00088}_{-0.0009}$	$0.0182^{+0.0025}_{-0.0022}$	$0.0232^{+0.0019}_{-0.0018}$
T_{14}	Total transit duration (days)	$0.04978^{+0.00051}_{-0.00053}$	$0.10815^{+0.00078}_{-0.00076}$	$0.08439^{+0.00062}_{-0.00064}$	$0.1796^{+0.0026}_{-0.0023}$	$0.1495^{+0.0017}_{-0.0016}$
b	Transit impact parameter	$1.024^{+0.061}_{-0.049}$	$0.078^{+0.081}_{-0.055}$	$0.8239^{+0.0056}_{-0.0062}$	$0.42^{+0.097}_{-0.15}$	$0.695^{+0.025}_{-0.028}$
ρ_P	Density (cgs)	$0.31^{+0.37}_{-0.18}$	$0.577^{+0.093}_{-0.086}$	$0.88^{+0.27}_{-0.26}$	$0.255^{+0.057}_{-0.049}$	$0.418^{+0.093}_{-0.083}$
$\log g_P$	Surface gravity (cgs)	$3.01^{+0.23}_{-0.24}$	$3.145^{+0.059}_{-0.065}$	$3.23^{+0.11}_{-0.15}$	$2.851^{+0.074}_{-0.078}$	$3.056^{+0.078}_{-0.088}$
M_P/M_*	Mass ratio	$0.001093^{+0.000088}_{-0.000084}$	$0.00082^{+0.00011}_{-0.0001}$	0.00069 ± 0.0002	$0.000507^{+0.000066}_{-0.000067}$	0.00071 ± 0.00012
d/R_*	Separation at midtransit	$4.97^{+0.36}_{-0.26}$	$8.08^{+0.36}_{-0.53}$	$13.95^{+0.84}_{-1.1}$	$6.51^{+0.57}_{-0.56}$	$7.75^{+0.58}_{-0.62}$

		TOI-3919	TOI-4153	TOI-5232	TOI-5301
Priors:					
π	Gaia parallax (mas)	$\mathcal{G}[1.6518, 0.0242]$	$\mathcal{G}[2.3867, 0.0201]$	$\mathcal{G}[1.6415, 0.0231]$	$\mathcal{G}[1.6998, 0.0501]$
[Fe/H]	Metallicity (dex)	$\mathcal{G}[0.2386, 0.1956]$	$\mathcal{G}[0.287, 0.1772]$	$\mathcal{G}[0.0365, 0.332]$	$\mathcal{G}[-0.1322, 0.1806]$
A_V	V-band extinction (mag)	$\mathcal{U}[0, 0.02666]$	$\mathcal{U}[0, 0.8091]$	$\mathcal{U}[0, 0.434]$	$\mathcal{U}[0, 0.18414]$
D_T	Dilution in TESS	$\mathcal{G}[0, 0.00047478]$	$\mathcal{G}[0, 0.00080667]$	$\mathcal{G}[0, 0.028318]$	$\mathcal{G}[0, 0.00040193]$

13

Table 6
(Continued)

		TOI-3919	TOI-4153	TOI-5232	TOI-5301
Stellar parameters:					
M_*	Mass ($M_\odot$)	$1.208^{+0.067}_{-0.07}$	$1.572^{+0.064}_{-0.071}$	$1.389^{+0.068}_{-0.075}$	$1.483^{+0.081}_{-0.14}$
R_*	Radius ($R_\odot$)	$1.319^{+0.052}_{-0.048}$	$1.605^{+0.048}_{-0.046}$	$1.785^{+0.067}_{-0.057}$	$2.19^{+0.12}_{-0.11}$
L_*	Luminosity ($L_\odot$)	$2.168^{+0.079}_{-0.077}$	$5.17^{+0.42}_{-0.55}$	$5.16^{+0.46}_{-0.53}$	$6.55^{+0.55}_{-0.5}$
ρ_*	Density (cgs)	$0.742^{+0.1}_{-0.093}$	$0.537^{+0.044}_{-0.046}$	$0.344^{+0.038}_{-0.042}$	$0.197^{+0.036}_{-0.032}$
$\log g$	Surface gravity (cgs)	$4.279^{+0.042}_{-0.044}$	$4.224^{+0.024}_{-0.029}$	$4.077^{+0.034}_{-0.042}$	$3.926^{+0.052}_{-0.061}$
$T_{\rm eff}$	Effective temperature (K)	6100 ± 110	6860^{+150}_{-180}	6500^{+180}_{-190}	6240 ± 160
[Fe/H]	Metallicity (dex)	$0.175^{+0.096}_{-0.094}$	$0.317^{+0.1}_{-0.13}$	$-0.104^{+0.11}_{-0.086}$	$0.03^{+0.13}_{-0.11}$
[Fe/H]$_0^\ddagger$	Initial metallicity	$0.208^{+0.08}_{-0.078}$	$0.39^{+0.072}_{-0.098}$	$0.04^{+0.093}_{-0.084}$	$0.11^{+0.12}_{-0.1}$
Age	Age (Gyr)	$3.1^{+1.9}_{-1.7}$	$0.4^{+0.53}_{-0.28}$	$2.37^{+0.53}_{-0.56}$	$2.43^{+1.1}_{-0.47}$
EEP	Equivalent evolutionary phase	368^{+40}_{-35}	308^{+24}_{-38}	378^{+24}_{-23}	401^{+49}_{-18}
A_V	V-band extinction (mag)	$0.0142^{+0.0086}_{-0.0094}$	$0.686^{+0.083}_{-0.12}$	$0.357^{+0.055}_{-0.097}$	$0.136^{+0.036}_{-0.066}$
d	Distance (pc)	$605.2^{+8.8}_{-8.7}$	419.1 ± 3.5	$609.0^{+8.6}_{-8.3}$	587.0^{+18}_{-17}
Planetary parameters:					
P	Period (days)	7.433234 ± 0.000014	4.6174141 ± 0.0000015	4.0966692 ± 0.0000067	5.858858 ± 0.000016
R_P	Radius (R_J)	$1.099^{+0.052}_{-0.05}$	$1.438^{+0.045}_{-0.042}$	$1.14^{+0.051}_{-0.045}$	$1.177^{+0.079}_{-0.072}$
M_P	Mass (M_J)	3.88 ± 0.23	1.15 ± 0.18	2.34 ± 0.16	$3.65^{+0.38}_{-0.39}$
T_C	Time of conjunction (BJD$_{\rm TDB}$)	2458954.374 ± 0.0013	$2459026.05484 \pm 0.00022$	$2459440.0678^{+0.00086}_{-0.00087}$	$2459494.1476^{+0.0011}_{-0.0012}$
T_0	Optimal conjunction time (BJD$_{\rm TDB}$)	$2459519.29976^{+0.00081}_{-0.0008}$	$2459557.05746 \pm 0.00015$	$2459857.92806^{+0.00052}_{-0.00053}$	2459277.3698 ± 0.001
a	Semimajor axis (au)	$0.0795^{+0.0014}_{-0.0016}$	$0.06311^{+0.00084}_{-0.00096}$	$0.05593^{+0.0009}_{-0.001}$	$0.0726^{+0.0013}_{-0.0024}$
i	Inclination (deg)	$86.98^{+0.2}_{-0.23}$	$88.75^{+0.76}_{-0.6}$	$88.3^{+1.1}_{-1.3}$	$83.1^{+1.8}_{-1.2}$
e	Eccentricity	$0.259^{+0.033}_{-0.036}$	$0.039^{+0.047}_{-0.028}$	$0.035^{+0.034}_{-0.024}$	$0.33^{+0.11}_{-0.1}$
ω_*	Argument of periastron (deg)	$-65.8^{+4.8}_{-3.4}$	-165.0^{+110}_{-100}	46.0^{+61}_{-77}	75.0^{+13}_{-14}
$T_{\rm eq}$	Equilibrium temperature (K)	1198.0^{+15}_{-14}	1669.0^{+29}_{-39}	1772.0^{+40}_{-45}	1655.0^{+39}_{-34}
$\tau_{\rm circ}$	Tidal circularization timescale (Gyr)	$22.5^{+6.3}_{-5}$	0.56 ± 0.13	$2.03^{+0.5}_{-0.47}$	$3.8^{+3.6}_{-2.2}$
K	RV semiamplitude (m s^{-1})	367^{+18}_{-17}	103 ± 16	239^{+15}_{-14}	337^{+35}_{-33}
R_P/R_*	Radius of planet in stellar radii	0.0856 ± 0.0017	$0.0921^{+0.00039}_{-0.00033}$	0.0656 ± 0.0014	$0.0552^{+0.0015}_{-0.0014}$
a/R_*	Semimajor axis in stellar radii	12.95 ± 0.56	$8.46^{+0.22}_{-0.25}$	$6.74^{+0.24}_{-0.28}$	7.11 ± 0.41
Depth	TESS flux decrement at midtransit	0.00695 ± 0.00026	$0.009323^{+0.000071}_{-0.000069}$	0.0048 ± 0.00021	$0.003254^{+0.000095}_{-0.000094}$
τ	Ingress/egress transit duration (days)	$0.0371^{+0.0036}_{-0.0033}$	$0.01642^{+0.0008}_{-0.0005}$	$0.01282^{+0.0008}_{-0.00054}$	$0.0134^{+0.0044}_{-0.0038}$
T_{14}	Total transit duration (days)	$0.1606^{+0.0031}_{-0.0029}$	$0.18801^{+0.00074}_{-0.0006}$	$0.1993^{+0.0016}_{-0.0014}$	$0.1645^{+0.0047}_{-0.0042}$
b	Transit impact parameter	$0.835^{+0.014}_{-0.016}$	$0.184^{+0.091}_{-0.11}$	$0.19^{+0.14}_{-0.13}$	$0.61^{+0.11}_{-0.23}$
ρ_P	Density (cgs)	$3.63^{+0.6}_{-0.53}$	$0.477^{+0.087}_{-0.085}$	$1.96^{+0.28}_{-0.27}$	$2.77^{+0.68}_{-0.57}$
$\log g_P$	Surface gravity (cgs)	$3.901^{+0.048}_{-0.051}$	$3.137^{+0.067}_{-0.08}$	$3.649^{+0.043}_{-0.048}$	$3.814^{+0.072}_{-0.076}$
M_P/M_*	Mass ratio	$0.00307^{+0.00016}_{-0.00015}$	0.0007 ± 0.00011	$0.00161^{+0.00011}_{-0.0001}$	0.00238 ± 0.00023
d/R_*	Separation at midtransit	$15.8^{+1}_{-1.1}$	8.48 ± 0.46	$6.64^{+0.37}_{-0.47}$	$4.81^{+0.86}_{-0.84}$

Notes. The priors listed at the top of the table are labeled as $\mathcal{G}$[mean, standard deviation] if they are Gaussian priors and $\mathcal{U}$[lower limit, upper limit] if they are uniform priors.

[a] Initial metallicity represents the metallicity of the star at formation.

[b] TOI-1855's transit is grazing, and as a consequence, the radius measurement is highly uncertain.
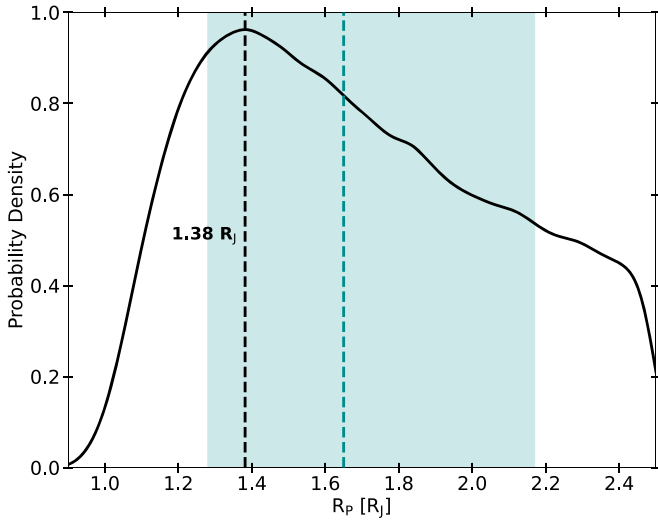
Figure 3. Posterior pdf of TOI-1855 b's radius. The black, labeled, vertical dashed line represents the posterior mode, $1.38R_J$. The cyan vertical dashed line and shaded region represent the median and 68% confidence interval, $1.65^{+0.52}_{-0.37}R_J$. The allowed planetary radius was constrained by an upper limit of $2.5R_J$.

TOI-3894 b, TOI-3919 b, TOI-4153 b, TOI-5232 b, and TOI-5301 b) detected by TESS, orbiting FGK stars. These planets range in mass between $0.554M_J$ and $3.88M_J$ and range in size between $0.967R_J$ and $1.438R_J$. The stars they orbit are all brighter than $G = 12.7$, which makes them suitable for further follow-up from a variety of ground-based facilities.

The median values and uncertainties of relevant stellar and planetary parameters from our EXOFASTv2 global fits are presented in Table 6.

4.1. TOI-1855 b's grazing transit

One of our planets, TOI-1855 b, exhibits a V-shaped transit caused by the planet only grazing the limb of the star. This transit shape is similar to what is usually seen for an eclipsing binary. Because of this, we paid special attention to TOI-1855 to ensure that our interpretation of it as a transiting giant planet is correct. TOI-1855 was observed by three different speckle instruments with four different filters and by two different AO instruments in three different filters. These observations detected a stellar companion, previously identified by Gaia (TIC 81247738), at a separation of 12″352 with a TESS magnitude of 13.524 ($\Delta T = 2.82$ mag). No other stellar companions were detected by any of the six HRI instruments. While these sources are blended in the TESS observations, the Bergeron, MuSCAT, MuSCAT2, LCO-CTIO, and SOAR observations used uncontaminated apertures and confirmed the transit signal to be on target. Additionally, the TESS data are corrected for contamination by both the SPOC and QLP pipelines (see Section 2.1), and we leave the dilution term for the TESS light curves as a free parameter in our EXOFASTv2 global fits (see Section 3) to account for possible errors in the dilution correction.

Another indicator of a blended eclipsing binary that is visible in the TESS data is a centroid offset, where the position of the target star appears to change as the stars enter an eclipse (Batalha et al. 2010). We find from the data validation report[60]

(MAST 2021a) for the SPOC-processed TESS Sector 50 data that the measured centroid offset is $0″408 \pm 2″55$, well within the expected variance and therefore consistent with no centroid offset. Additionally, we searched the TESS data for evidence of a secondary eclipse, another sign of an eclipsing binary, by phasing the TESS data on the optimal ephemeris from our EXOFASTv2 global fit and binning the phased light curve. We find no evidence of a secondary eclipse in either sector of data. Finally, we find no evidence of chromaticity, another common indicator for an eclipsing binary. The combination of an RV orbit, HRI nondetection, secondary eclipse nondetection, and the lack of a centroid offset and chromaticity implies that it is highly unlikely that TOI-1855 b's transit signal is the consequence of an eclipsing binary.

The other difficulty raised by the grazing configuration of TOI-1855 b's transit is that we are unable to precisely constrain its radius from the transit alone. In Section 3.1, we discussed the R_P upper limit placed on TOI-1855's fit and the resulting posterior mode, $1.38R_J$. In order to get a different constraint on the radius of TOI-1855 b, we used the code Forecaster[61] from Chen & Kipping (2017) to generate a probability density function (pdf) of the radius of TOI-1855 given its mass distribution from our EXOFASTv2 global fit. From this mass–radius relation alone, we find a median planetary radius of $1.21R_J \pm 0.21R_J$, which is consistent within 1σ with the posterior mode ($1.38R_J$) and the median ($1.65^{+0.52}_{-0.37}$) from the fit. Forecaster is built from a sample of planets with a wide range of isolations, but it is possible that TOI-1855 b's size could be underestimated by using only Forecaster if its radius is inflated by insolation.

4.2. Bimodal Solutions

Two of our EXOFASTv2 global fits converged on solutions that had bimodal posterior distributions in stellar mass and age: TOI-3894 and TOI-5301. In order to characterize each individual solution from both fits, we split the pdf's of TOI-3894's and TOI-5301's fits, identifying a solution with a higher stellar mass and a separate solution with a lower stellar mass for each (see Figure 4). For TOI-3894, if we separate the pdf using a stellar mass of 1.145 $M_\odot$ (the center of the valley between the two peaks in Figure 4), the EXOFASTv2 global fit slightly favors the lower-mass solution ($M_\star = 1.089^{+0.038}_{-0.051}$ $M_\odot$, age $= 7.2^{+1.7}_{-1.1}$ Gyr), with a probability of 53.0%. In the case of TOI-5301, we split the pdf using a stellar mass of 1.375 $M_\odot$ and find that the higher-mass solution ($M_\star = 1.507^{+0.068}_{-0.067}$ $M_\odot$, age $= 2.29^{+0.42}_{-0.42}$ Gyr) is favored, with a probability of 78.3%. Both of these uncertain fits are consequences of the stars' observed parameters indicating that they are near an evolutionary transition. To encapsulate both possibilities in both systems, we present the median and standard deviation of each parameter for the higher- and lower-mass solutions of both targets in Table 7.

4.3. Lithium in TOI-5301

While vetting the spectra of the stars in our sample, we discovered a discernible lithium absorption feature in the spectra of TOI-5301. The strength of a star's lithium absorption feature serves as a valuable tool to determine stellar age (e.g., Vauclair 1972). This feature is also useful in identifying

---

[60] https://tev.mit.edu/data/delivered-signal/i244634/

[61] https://github.com/chenjj2/forecaster
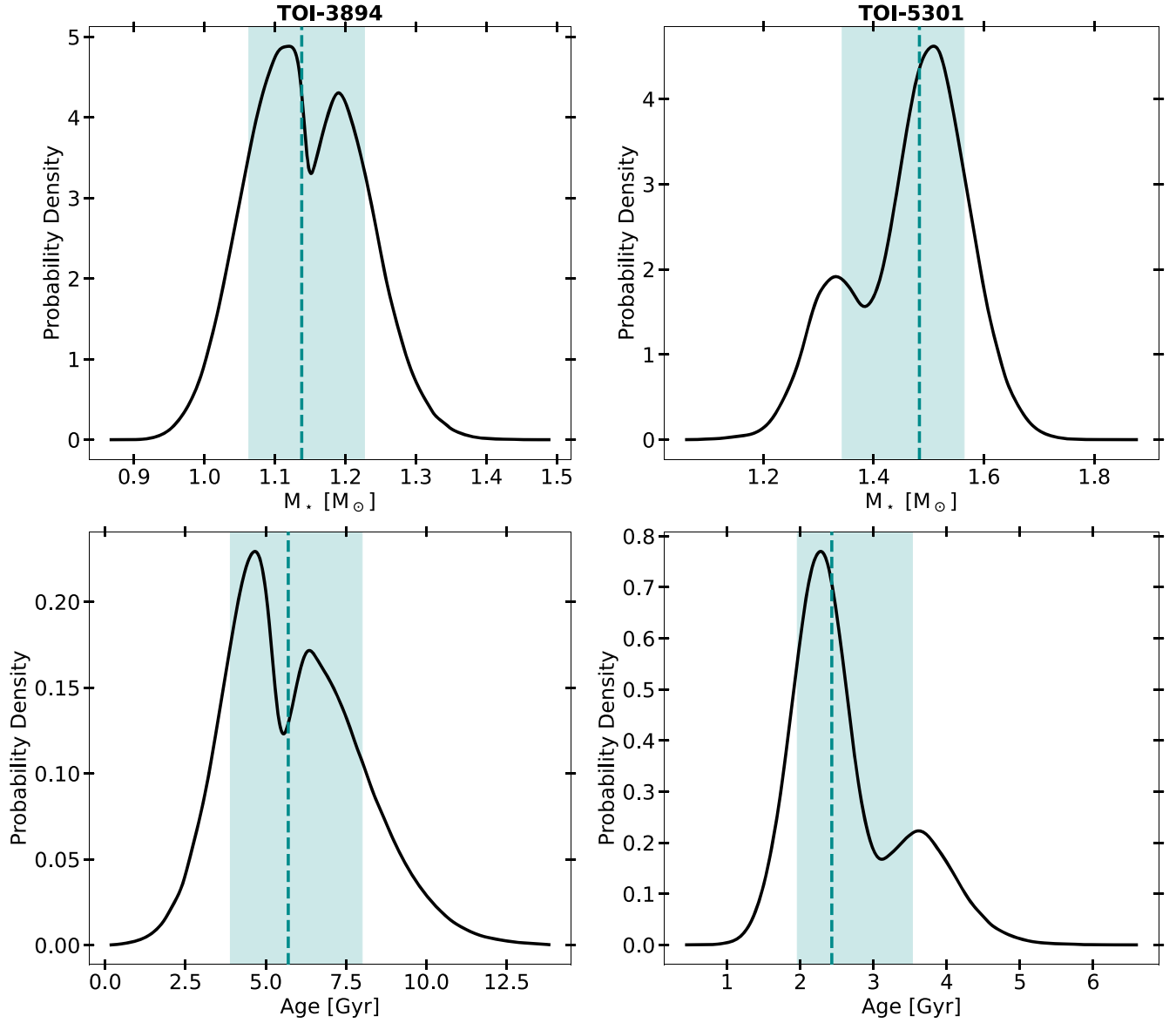
Figure 4. Gaussian kernel density estimations of TOI-3894's (left) and TOI-5301's (right) stellar mass and age posterior distributions from our `EXOFASTv2` global fits, illustrating a bimodal distribution in both parameters. The cyan dashed line indicates the median value of each parameter, while the shaded region represents the 68% confidence region. The normalized probability densities were estimated using the Gaussian kernel density estimator in the Python package `scipy.stats`. TOI-3894's fit slightly favored the lower-mass solution, with a probability of 53.0%, while TOI-5301's fit favored the higher-mass solution, with a probability of 78.3%.

instances where a star may have ingested planets (Montalbán & Rebolo [2002](#)), particularly among stars that share similar mass and evolutionary stages to those of TOI-5301 (e.g., Soares-Furtado et al. [2021](#)).

Is the lithium abundance of our target unusual when compared to a control sample of stars? To answer this question, we performed a lithium abundance analysis of the target by coadding 19 TRES observations taken between 2022 September 1 and 2022 November 9. Before coadding the spectra to build up the SNR, each spectrum was continuum normalized, barycenter corrected, and Doppler corrected. Following the procedures outlined in Jeffries et al. ([2023](#)), we measured the equivalent width of the lithium absorption doublet (Li I) at 6707.8 Å. We measure an SNR per resolution element of 84 for the coadded spectra, where the width of each resolution element is 2 pixels, or 6.8 km s^{-1}. Using `pymoog`[62]

and `pyMOOGi`,[63] we measured a lithium abundance on the 12-point scale of $A(\mathrm{Li}) = 2.47 \pm 0.04$ dex.

To determine whether this measured abundance strength is unusual, we compared this value to the lithium abundances of an ensemble of 392 control sample stars with reported lithium abundance measurements in the GALAH DR3 database (Buder et al. [2021](#)). We selected control stars that exhibited stellar properties akin to that of our target. This included stars with a surface gravity of 3.9 ± 0.05 dex, an effective temperature of 6260 ± 50 K, an iron abundance ([Fe/H]) of -0.046 ± 0.05 dex, and a Gaia RUWE value <1.4, which indicates that the target is less likely to be part of a binary system (Belokurov et al. [2020](#)).

The lithium abundances of our control population present a skewed lithium distribution. Therefore, we computed a

---

Table 7
Median Values and 68% Confidence Intervals for Bimodal Fits

		TOI-3894		TOI-5301	
		Low-mass Solution (53.0% Probability)	High-mass Solution (47.0% Probability)	Low-mass Solution (21.7% Probability)	High-mass Solution (78.3% Probability)
Stellar parameters:					
M_*	Mass ($M_\odot$)	$1.089^{+0.038}_{-0.051}$	$1.206^{+0.052}_{-0.039}$	$1.316^{+0.039}_{-0.05}$	$1.507^{+0.068}_{-0.067}$
R_*	Radius ($R_\odot$)	$1.506^{+0.057}_{-0.052}$	$1.498^{+0.053}_{-0.054}$	$2.23^{+0.12}_{-0.11}$	2.18 ± 0.11
L_*	Luminosity ($L_\odot$)	$2.621^{+0.094}_{-0.083}$	$2.627^{+0.091}_{-0.082}$	$6.48^{+0.59}_{-0.52}$	$6.57^{+0.54}_{-0.49}$
ρ_*	Density (cgs)	$0.447^{+0.054}_{-0.051}$	$0.507^{+0.062}_{-0.05}$	$0.167^{+0.026}_{-0.024}$	$0.205^{+0.034}_{-0.028}$
$\log g$	Surface gravity (cgs)	$4.117^{+0.035}_{-0.039}$	$4.169^{+0.036}_{-0.031}$	$3.859^{+0.042}_{-0.046}$	$3.939^{+0.046}_{-0.042}$
$T_{\rm eff}$	Effective temperature (K)	5990.0 ± 110	6010.0 ± 110	6170.0 ± 160	6260.0^{+160}_{-150}
[Fe/H]	Metallicity (dex)	$0.01^{+0.073}_{-0.054}$	$0.038^{+0.092}_{-0.069}$	$-0.02^{+0.1}_{-0.11}$	$0.05^{+0.13}_{-0.11}$
[Fe/H]$_0$	Initial metallicity	$0.08^{+0.064}_{-0.055}$	$0.117^{+0.075}_{-0.062}$	$0.036^{+0.085}_{-0.095}$	$0.13^{+0.12}_{-0.099}$
Age	Age (Gyr)	$7.2^{+1.7}_{-1.1}$	$4.27^{+0.74}_{-1}$	$3.78^{+0.49}_{-0.39}$	$2.29^{+0.42}_{-0.4}$
EEP	Equal evolutionary phase	$440.8^{+7.9}_{-9.3}$	405.0^{+13}_{-23}	$453.7^{+4.1}_{-6.3}$	397.0^{+11}_{-17}
A_V	V-band extinction (mag)	0.019 ± 0.013	$0.021^{+0.012}_{-0.014}$	$0.113^{+0.051}_{-0.068}$	$0.141^{+0.032}_{-0.062}$
d	Distance (pc)	$411.6^{+3.9}_{-3.8}$	$412.1^{+3.9}_{-3.8}$	585.0^{+17}_{-16}	588.0^{+18}_{-17}
Planetary parameters:					
P	Period (days)	4.33454 ± 0.0000022	4.3345401 ± 0.0000022	$5.858857^{+0.000016}_{-0.000017}$	5.858858 ± 0.000016
R_P	Radius (R_J)	$1.363^{+0.055}_{-0.051}$	$1.352^{+0.053}_{-0.052}$	$1.207^{+0.081}_{-0.073}$	$1.168^{+0.076}_{-0.07}$
M_P	Mass (M_J)	0.82 ± 0.14	0.88 ± 0.15	3.4 ± 0.33	3.72 ± 0.37
T_C	Time of conjunction (BJD$_{\rm TDB}$)	$2458912.41365^{+0.00041}_{-0.00043}$	$2458912.41361^{+0.0004}_{-0.00042}$	$2459494.1476^{+0.0012}_{-0.0013}$	$2459494.1476^{+0.0011}_{-0.0012}$
T_0	Optimal conjunction time (BJD$_{\rm TDB}$)	$2459250.50777^{+0.00037}_{-0.00038}$	$2459250.50773^{+0.00035}_{-0.00038}$	$2459277.3699^{+0.001}_{-0.0011}$	$2459277.36981 \pm 0.00099$
a	Semimajor axis (au)	$0.05354^{+0.00061}_{-0.00085}$	$0.05539^{+0.00079}_{-0.0006}$	$0.06975^{+0.00068}_{-0.00089}$	0.073 ± 0.0011
i	Inclination (deg)	$84.63^{+0.4}_{-0.46}$	$85.08^{+0.37}_{-0.36}$	$82.0^{+1.4}_{-1.1}$	$83.3^{+1.9}_{-1}$
e	Eccentricity	$0.05^{+0.052}_{-0.035}$	$0.046^{+0.052}_{-0.032}$	$0.337^{+0.12}_{-0.099}$	$0.33^{+0.11}_{-0.1}$
ω_*	Argument of periastron (deg)	108.0^{+89}_{-93}	-140.0 ± 100	76.0 ± 13	75.0^{+13}_{-14}
$T_{\rm eq}$	Equilibrium temperature (K)	1531.0^{+17}_{-15}	1504.0 ± 15	1682.0^{+38}_{-34}	1648.0^{+34}_{-31}
$\tau_{\rm circ}$	Tidal circularization timescale (Gyr)	$0.304^{+0.093}_{-0.081}$	$0.365^{+0.1}_{-0.086}$	$2.7^{+2.5}_{-1.7}$	$4.2^{+3.8}_{-2.4}$
K	RV semiamplitude (m s^{-1})	96.0 ± 16	96.0 ± 16	338.0^{+36}_{-33}	336.0^{+34}_{-33}
R_P/R_*	Radius of planet in stellar radii	$0.09302^{+0.00077}_{-0.00079}$	$0.09275^{+0.00077}_{-0.00078}$	$0.0557^{+0.0015}_{-0.0016}$	$0.0551^{+0.0015}_{-0.0014}$
a/R_*	Semimajor axis in stellar radii	$7.63^{+0.29}_{-0.3}$	$7.96^{+0.31}_{-0.3}$	$6.72^{+0.33}_{-0.34}$	$7.2^{+0.38}_{-0.34}$
Depth	TESS flux decrement at midtransit	$0.008978^{+0.000089}_{-0.00009}$	$0.008969^{+0.00009}_{-0.000091}$	$0.003269^{+0.000093}_{-0.000096}$	$0.00325^{+0.000095}_{-0.000093}$
τ	Ingress/egress transit duration (days)	0.0235 ± 0.0018	$0.0228^{+0.0018}_{-0.0017}$	$0.0149^{+0.0045}_{-0.0043}$	$0.013^{+0.0042}_{-0.0036}$
T_{14}	Total transit duration (days)	0.1498 ± 0.0016	$0.1492^{+0.0016}_{-0.0015}$	0.166 ± 0.0047	$0.1641^{+0.0046}_{-0.0041}$
b	Transit impact parameter	$0.7^{+0.023}_{-0.028}$	$0.689^{+0.025}_{-0.028}$	$0.655^{+0.088}_{-0.19}$	$0.6^{+0.11}_{-0.23}$
ρ_P	Density (cgs)	$0.4^{+0.087}_{-0.078}$	$0.44^{+0.095}_{-0.084}$	$2.39^{+0.55}_{-0.47}$	$2.88^{+0.67}_{-0.54}$
$\log g_P$	Surface gravity	$3.039^{+0.076}_{-0.087}$	$3.076^{+0.075}_{-0.085}$	$3.76^{+0.067}_{-0.07}$	$3.828^{+0.067}_{-0.069}$
M_P/M_*	Mass ratio	0.00073 ± 0.00012	0.00069 ± 0.00012	$0.00248^{+0.00023}_{-0.00024}$	$0.00236^{+0.00022}_{-0.00023}$
d/R_*	Separation at midtransit	$7.51^{+0.49}_{-0.64}$	$8.0^{+0.61}_{-0.47}$	$4.49^{+0.76}_{-0.84}$	$4.91^{+0.86}_{-0.83}$

modified Z-score,

$$Z = \frac{0.6745 \times (X_i - {\rm Median}(X))}{\rm MAD}, \qquad (1)$$

which incorporates the median and absolute deviation from the median (MAD) for the control sample lithium abundances, as opposed to the population mean and standard deviation. Our target's modified Z-score is measured at 0.003, suggesting that its lithium abundance is nearly identical to the median of our data set. Therefore, we report no indication of abnormal lithium contamination in the spectra of TOI-5301.

4.4. Early Trends in the Hot Jupiter Population

The purpose of this survey is to generate a large, complete sample in order to statistically assess the origins of HJs. As such, it is too early to make conclusive claims that require robust statistics. Instead, we argue that there are several tentative trends arising in the present sample of HJs.

First, it is notable that seven of our nine planets have orbits that are consistent with circular within 2.45σ (Lucy & Sweeney 1971) and are thus consistent with either migration mechanism: gas-disk migration or high-eccentricity tidal migration. Two of the planets in this sample, TOI-3919 b and TOI-5301 b, have significant eccentricities that cannot be explained by quiescent disk migration alone. TOI-3919's RVs show signs of a long-term trend that could be evidence of an outer companion and therefore a possible perturber to boost the eccentricity of TOI-3919 b and trigger high-eccentricity tidal migration. Both of these planets are shown in Figure 5 and compared to several different avenues and outcomes of planet migration. These two planets join the 55 other HJs with reported eccentricities $>3\sigma$ above zero (9.7% of the HJ population) per the NASA Exoplanet Archive[64] (date accessed: 2024
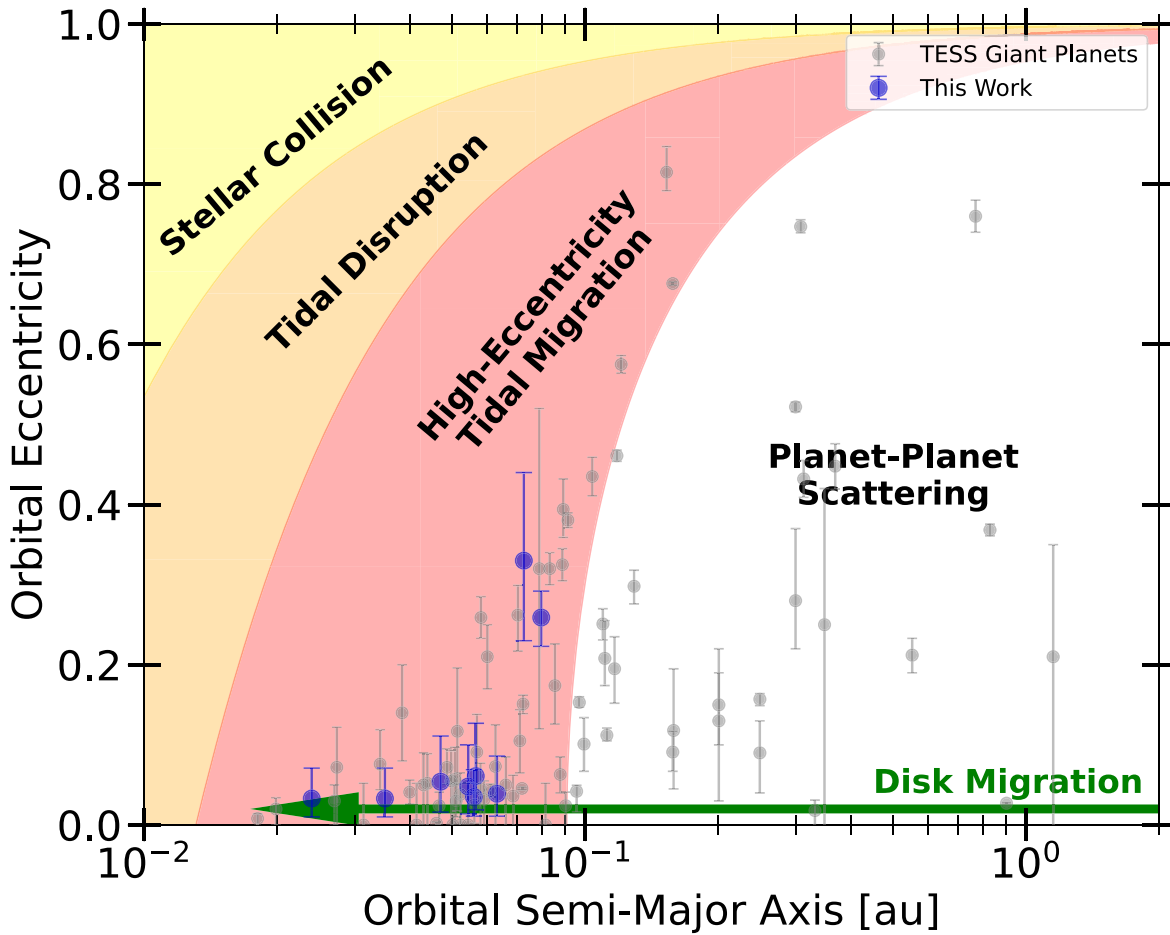
Figure 5. Eccentricity and semimajor-axis distribution of the planets discovered in this work, compared to giant planets in the literature and several avenues and outcomes of giant planet migration (similar to Figure 4 in Dawson & Johnson 2018). The region labeled "Stellar Collision" corresponds to a giant planet colliding with the star, assuming that the star is 1 $R_\odot$ in size. The region labeled "Tidal Disruption" corresponds to a Jupiter-like planet falling within the Roche limit of the Sun. Finally, the red region corresponds to the tidal circularization of a highly eccentric giant planet around a Sun-like star. The blue circles represent the EXOFASTv2 median semimajor axis and eccentricity of the planets in this work, while the gray circles represent substellar bodies discovered by TESS with masses between $0.25M_J$ and $13M_J$ and reported eccentricities, obtained from the NASA Exoplanet Archive. Many of the eccentric planets, including those that fall outside of the three shaded regions, can be explained by planet–planet scattering that has not yet or will not be tidally circularized. The equations that describe each of these shaded regions are shown in Dawson & Johnson (2018).

April 5). While the NASA Exoplanet Archive is a heterogeneous source of exoplanet parameters and should not be used to identify definitive trends, this is a significant minority of the population that must receive further scrutiny. Since many planets with periods less than 10 days are expected to have very short tidal circularization timescales (Adams & Laughlin 2006), the fraction of HJs that once had boosted eccentricities could be much larger than 9.7%. This implies that, at the very least, high-eccentricity tidal migration is an important migration mechanism that must be considered for a nonnegligible fraction of the HJ population. Bonomo et al. (2017), Rodriguez et al. (2023), and Zink & Howard (2023) all argue that the current eccentricity distribution of known HJs is consistent with high-eccentricity tidal migration being the dominant pathway for the evolution of HJs, an argument that can continue to be tested with a growing sample of HJs.

Additionally, two of the stars that we observed have long-term RV trends: TOI-2368 has a linear slope of 0.21 ± 0.11 m s^{-1} day^{-1}, and TOI-3919 has a slope of $-0.79^{+0.31}_{-0.30}$ m s^{-1} day^{-1}. If further RV follow-up reveals a continuation of the trend consistent with a giant substellar companion on a wide orbit, then these systems would be

further evidence that HJ-hosting systems are not always devoid of other planets, as RV surveys (e.g., Knutson et al. 2014; Bryan et al. 2016; Zink & Howard 2023) have argued. Zink & Howard (2023) also argue that the properties of systems hosting an HJ and a distant giant companion favor a scenario in which the HJ migrated via coplanar high-eccentricity tidal migration.

Several issues with high-eccentricity tidal migration have been raised, however, that must be addressed. For example, Socrates et al. (2012) argued that we should be able to detect a significant number of "super-eccentric" Jupiters that are actively migrating to become HJs, more than have yet been observed. Additionally, they argue that the tidal efficiency of HJs must be at least 10 times larger than Jupiter's. Further studies should address these issues and elucidate the importance of each mechanism of giant planet formation and evolution.

4.5. Building a Complete Sample of Hot Jupiters

The transit photometry, RV, SED, and MIST evolutionary plots for each system investigated within this work are organized by system and presented in Figures 6–14. This
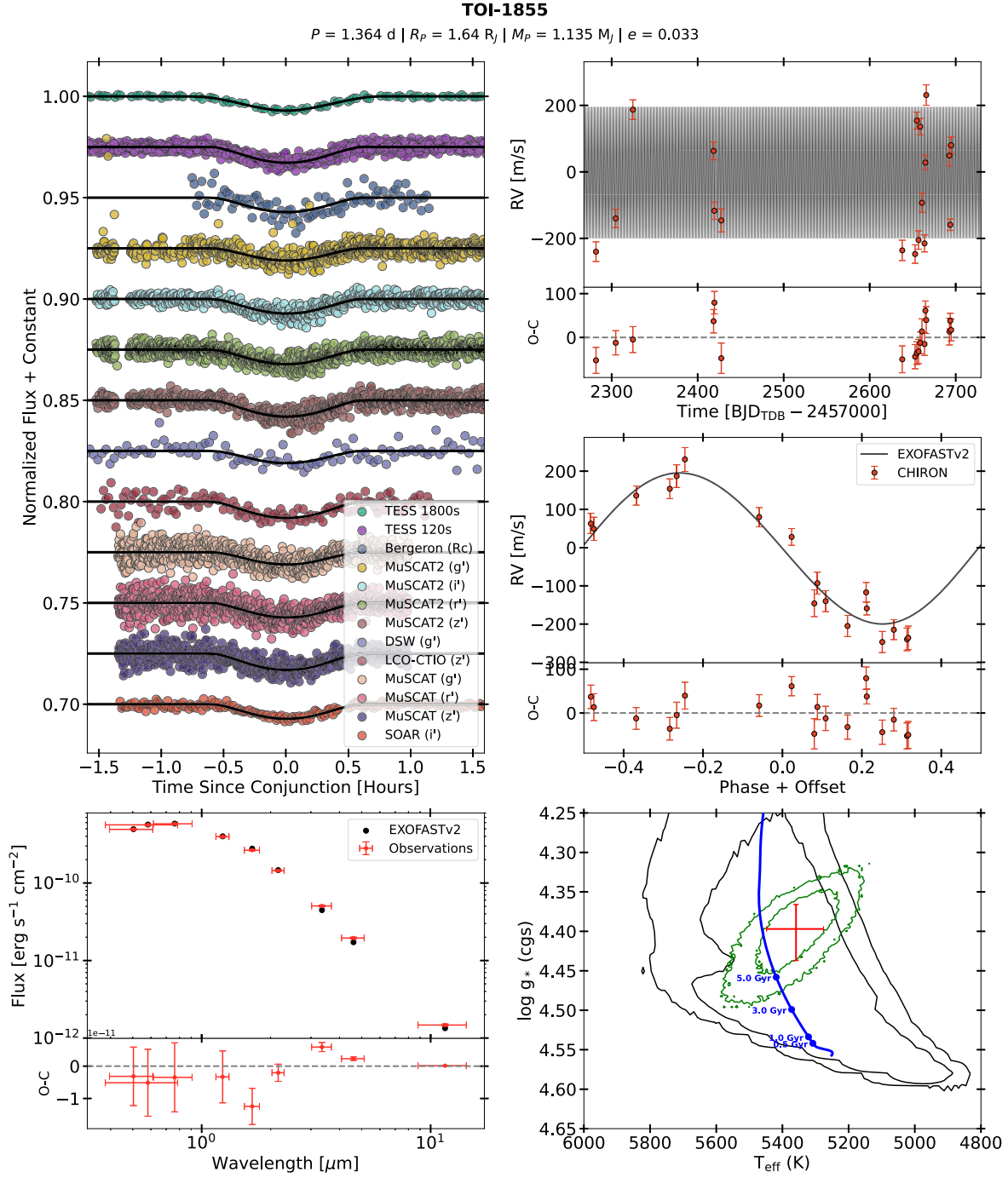
Figure 6. `TESS`, follow-up, and archival observations of TOI-1855 as they compare to the `EXOFASTv2` results. Top left: unbinned `TESS` and follow-up ground-based transits, phase-folded and shown in comparison to the best-fit time of conjunction with an arbitrary normalized flux offset. Multiple `TESS` sectors in the same cadence are stacked on top of each other. Bottom left: the SED of the target star compared to the best-fit `EXOFASTv2` model. Residuals are shown on a linear scale, using the same units as the primary y-axis. Top right: RV observations vs. time, including any significant long-term trend. The residuals are shown in the subpanel below in the same units. Middle right: RV observations phase-folded using the best-fit ephemeris from the `EXOFASTv2` global fit. The phase is shifted so that the transit occurs at Phase + Offset = 0. The residuals are shown in the subpanel below in the same units. Bottom right: the evolutionary track and current evolutionary stage of the planet according to the best-fit MIST model. The blue line indicates the best-fit MIST track, while the black contours show the 1σ and 2σ constraints on the star's current T_{eff} and log g from the MIST isochrone alone. The green contours represent the 1σ and 2σ constraints on the star's T_{eff} and log g from the `EXOFASTv2` global fit, combining constraints from observations of the star and planet. The red plus sign indicates the median and 68% confidence interval reported in Table 6.

paper is the first in a new series of papers aimed at constructing a homogeneously analyzed set of HJ parameters, built off of the works of Rodriguez et al. (2019, 2021, 2023), Ikwut-Ukwa et al. (2022), and Yee et al. (2022, 2023). Per Yee et al. (2021), roughly 300−400 transiting HJs around FGK stars with $G < 12.5$ mag should be discoverable with `TESS`, a sample

TOI-2107

$P = 2.455$ d | $R_P = 1.211$ R$_J$ | $M_P = 0.83$ M$_J$ | $e = 0.033$
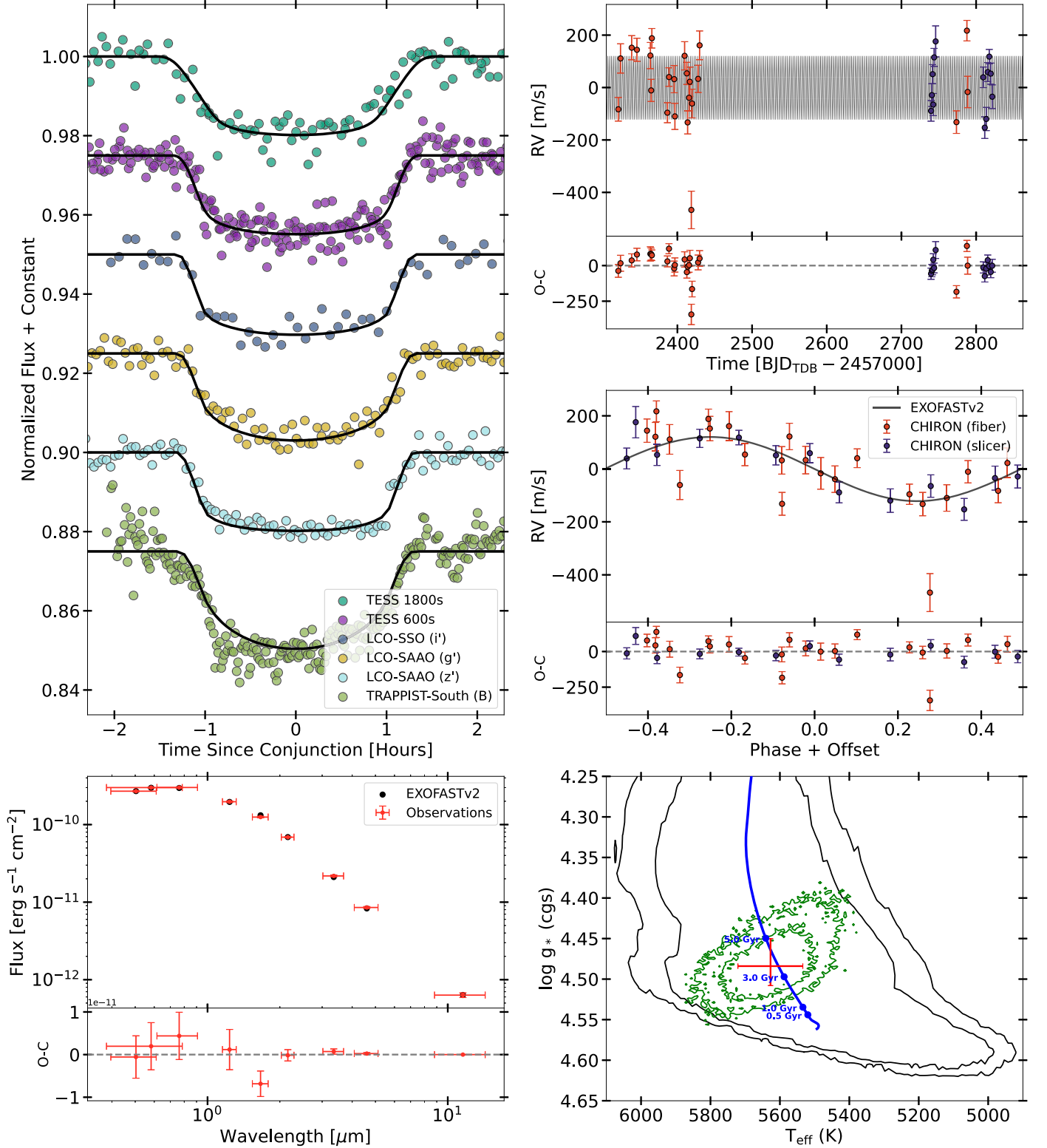
Figure 7. Same as Figure 6, but for TOI-2107.

that is now $\gtrsim 60\%$ complete. Once this sample is complete, which will be achievable within the next few years with the help of TESS and TFOP, it will be possible to carefully consider the different possible migration mechanisms of HJs using detailed statistics with well-quantified biases. Models of other physical processes, such as the radius inflation of HJs subject to high instellation, will also be easier to test with this complete sample.

TOI-2368

$P = 5.175$ d | $R_P = 0.967$ R$_J$ | $M_P = 0.65$ M$_J$ | $e = 0.061$
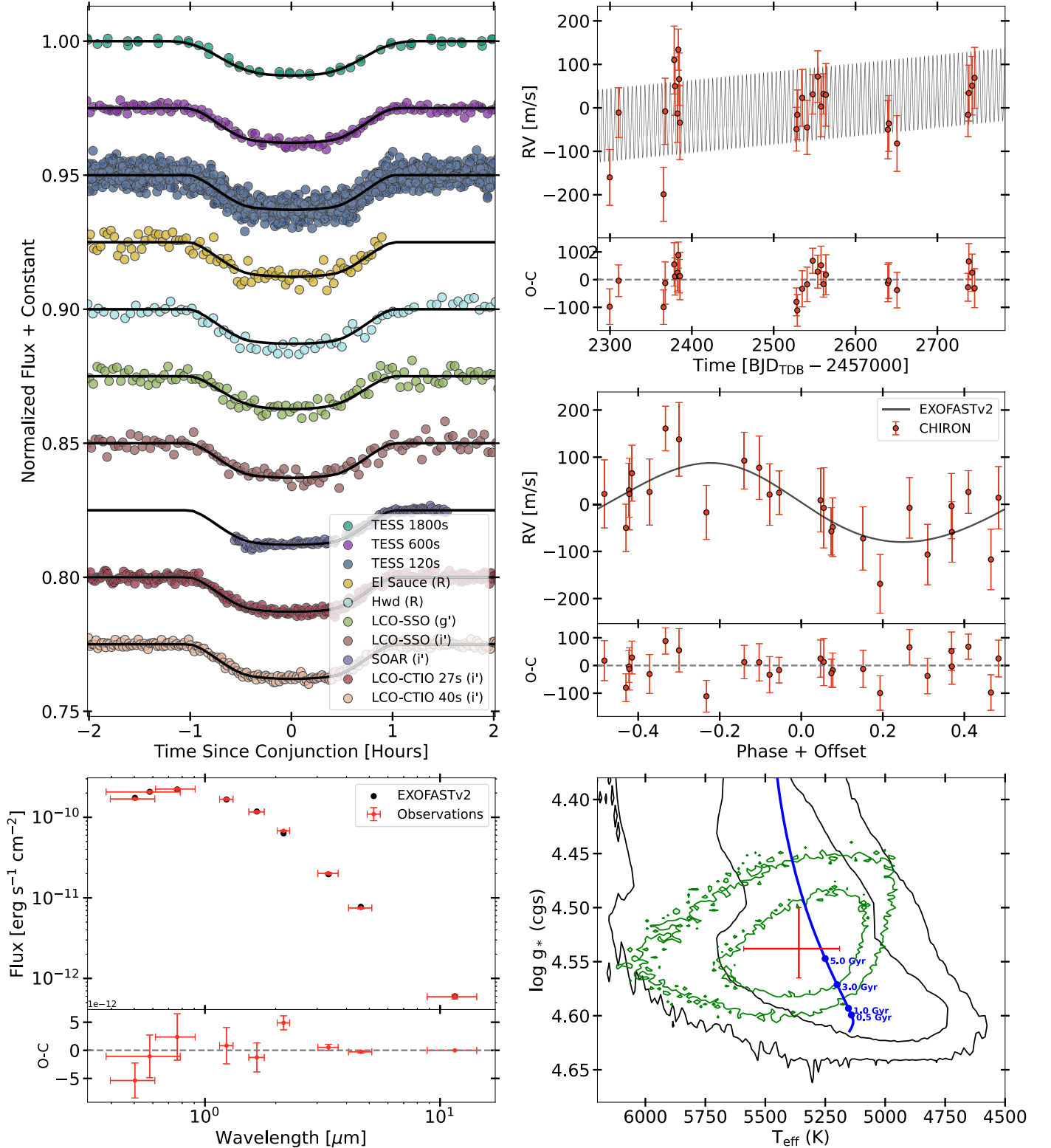
Figure 8. Same as Figure 6, but for TOI-2368. Notably, the best-fit RVs for TOI-2368 imply a linear RV trend of 0.21 ± 0.11 m s^{-1} day^{-1}, which was included in our fit per our prescription to fit for an RV trend if it is favored to greater than 1σ.

Individual discoveries of HJ systems with confounding features are constantly being made that will weigh on the models that we use to describe the evolution of systems with HJs

(e.g., Becker et al. 2015; Wittenmyer et al. 2022; Yoshida et al. 2023). For example, since HJs that underwent high-eccentricity tidal migration are unlikely to have nearby companions, due to the
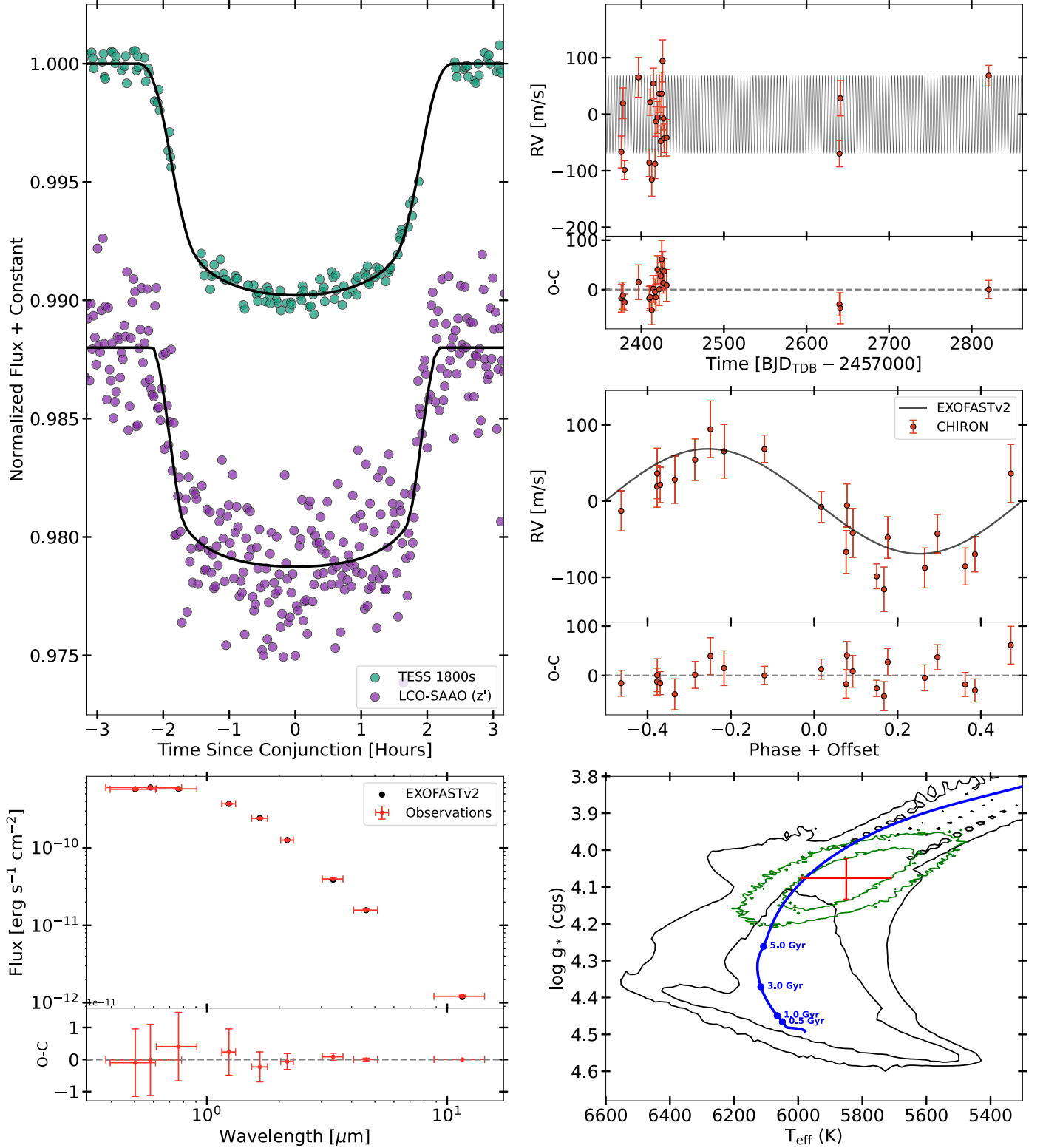
Figure 9. Same as Figure 6, but for TOI-3321.

high likelihood of ejections and engulfment (Mustill et al. 2015), the exceptions to this rule will be key systems to test models of gas-disk migration. Additionally, photometric (e.g., De et al. 2023)

and chemical (Montalbán & Rebolo 2002; see Section 4.3) signatures of planet engulfment may be found that provide insight into the stability of systems containing HJs. Throughout the

TOI-3894

$P = 4.335$ d | $R_P = 1.358$ R$_J$ | $M_P = 0.85$ M$_J$ | $e = 0.048$
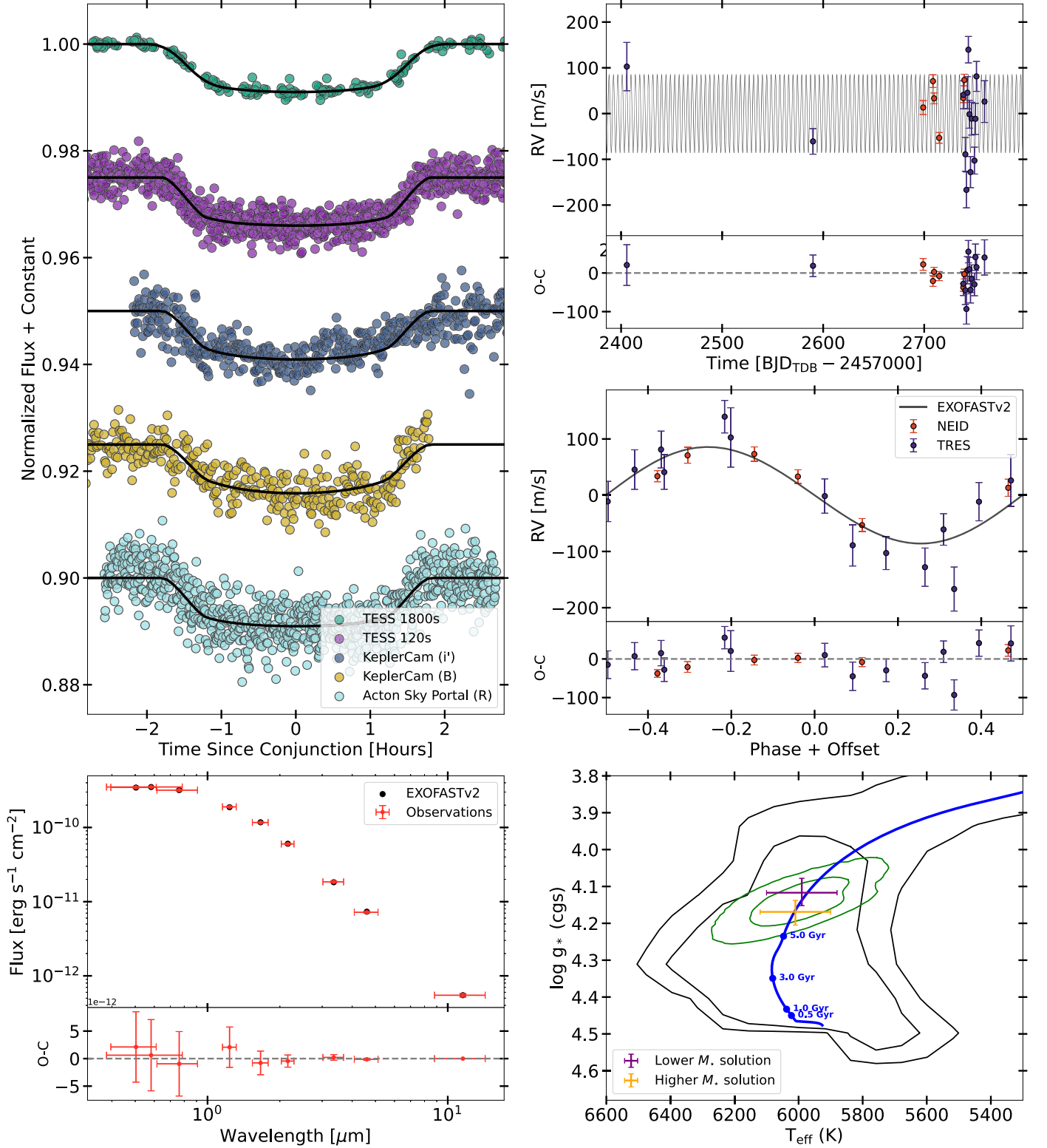
Figure 10. Same as Figure 6, but for TOI-3894. TOI-3894's `EXOFASTv2` global fit was bimodal in stellar mass and age. To represent both modes, we show median values and standard deviations from each stellar mass solution in the bottom right panel.

construction of the sample, we will give greater consideration and care to benchmark systems in order to generate further constraints on models of migration. It is with the combination of a statistical sample of systems hosting HJs and the careful consideration of these benchmark systems that we hope to gain further insight into the origins and evolution of the enigmatic population of HJs.

TOI-3919

$P = 7.433$ d | $R_P = 1.099$ R_J | $M_P = 3.88$ M_J | $e = 0.259$
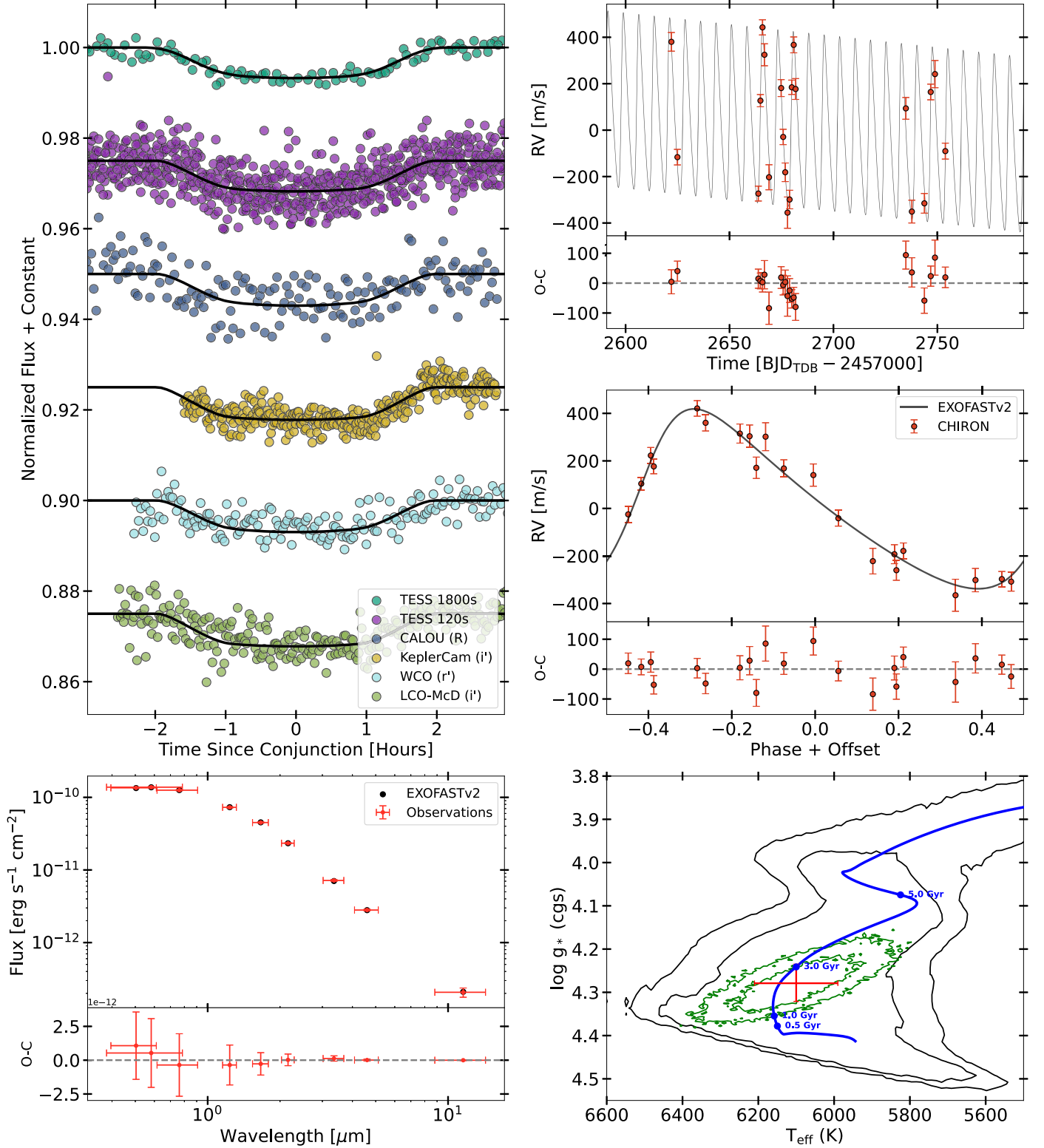
Figure 11. Same as Figure 6, but for TOI-3919. Notably, the best-fit RVs for TOI-3919 imply a linear RV trend of $-0.79^{+0.31}_{-0.30}$ m s^{-1} day^{-1}, which was included in our fit per our prescription to fit for an RV trend if it is favored to greater than 1σ.

5. Summary

In this article, we present nine new HJs discovered by NASA's TESS mission as part of an ongoing effort to discover and characterize all HJs orbiting FGK stars brighter than $G = 12.5$ mag. This article is the first in a series of articles titled "Migration and Evolution of giant ExoPlanets (MEEP)."

TOI-4153

$P = 4.617$ d | $R_P = 1.438$ R$_J$ | $M_P = 1.15$ M$_J$ | $e = 0.039$
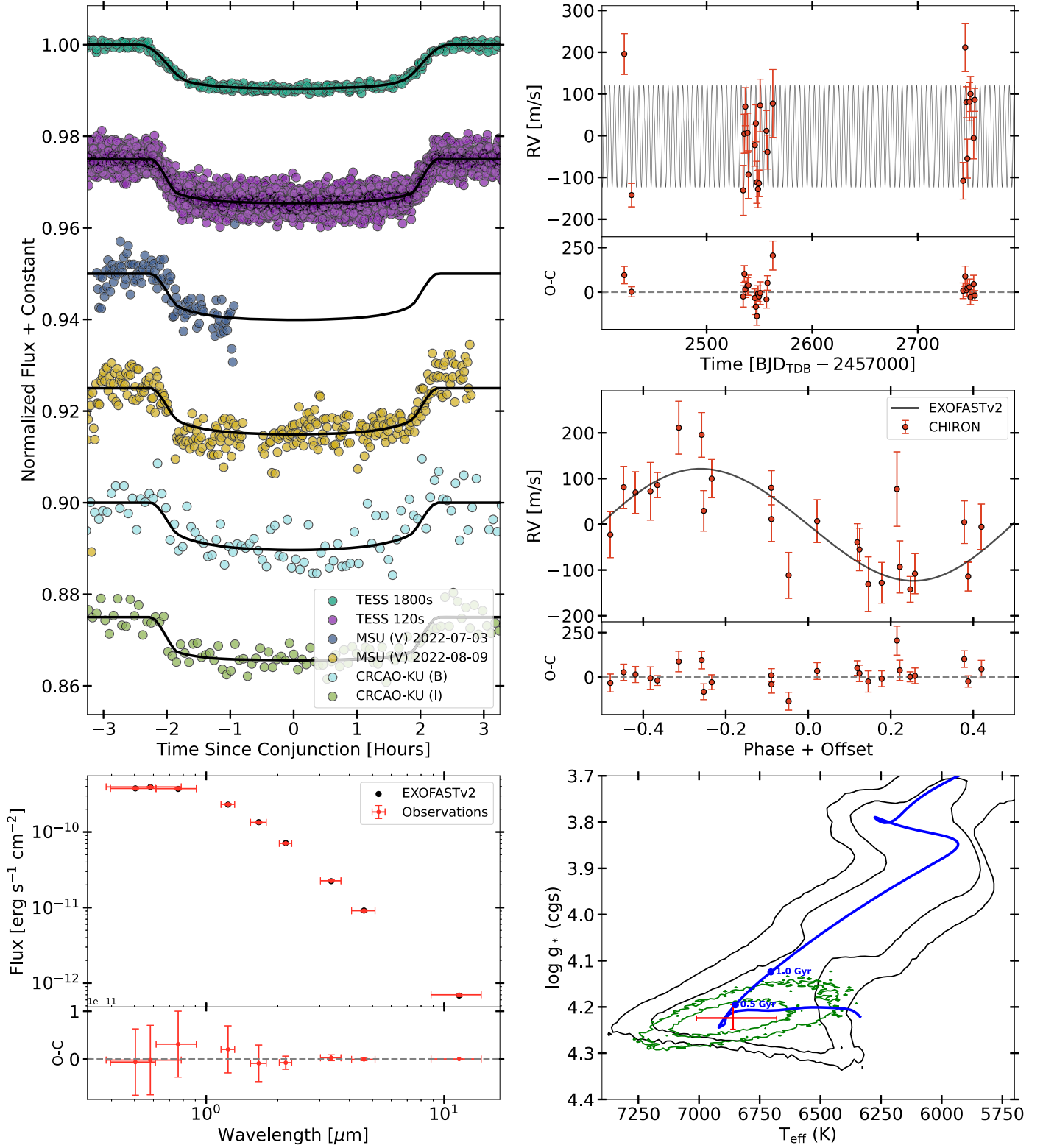
Figure 12. Same as Figure 6, but for TOI-4153.

This effort aims to use homogenous detection and analysis techniques to generate a population of HJs with well-quantified selection biases. In pursuit of this effort, we are obtaining precise eccentricities, along with a host of other important parameters (such as planetary and stellar mass and radius), to test theories of giant planet formation and evolution.

The HJs we present in this work have masses ranging from $0.554^{+0.076}_{-0.075}M_J$ to $3.88M_J \pm 0.23M_J$ and radii ranging from

TOI-5232

$P = 4.097$ d | $R_P = 1.14$ R$_J$ | $M_P = 2.34$ M$_J$ | $e = 0.035$
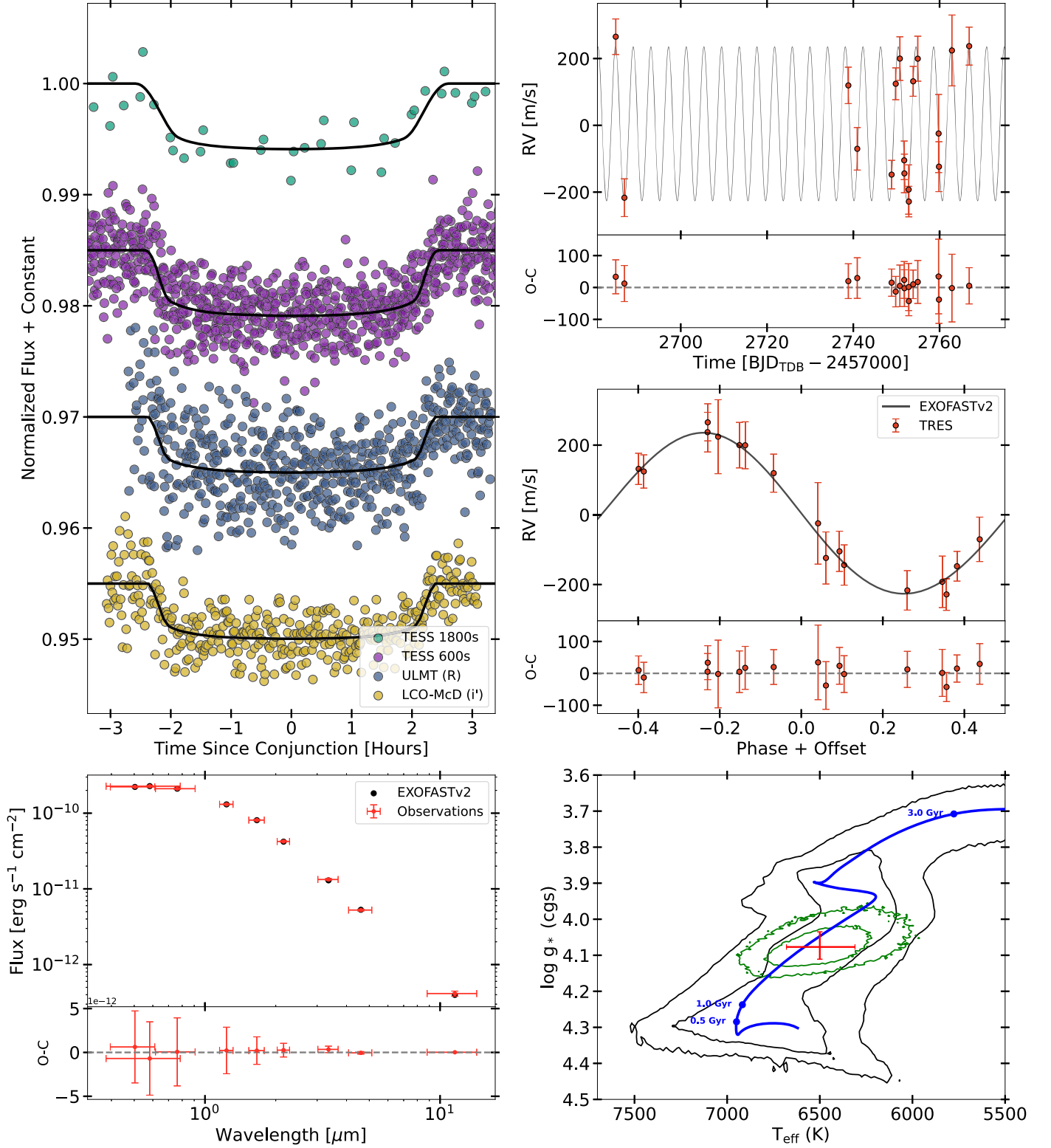
Figure 13. Same as Figure 6, but for TOI-5232.

$0.967^{+0.036}_{-0.031}R_{\mathrm{J}}$ to $1.438^{+0.045}_{-0.042}R_{\mathrm{J}}$, excluding the one planet in our sample that exhibits a grazing transit and for which the radius cannot be precisely constrained. Two of the planets in our sample,

TOI-3919 b and TOI-5301 b, exhibit significant orbital eccentricities that imply that they may have undergone high-eccentricity tidal migration. We investigated the lithium absorption feature of

TOI-5301

$P = 5.859$ d | $R_P = 1.177$ R$_J$ | $M_P = 3.65$ M$_J$ | $e = 0.33$
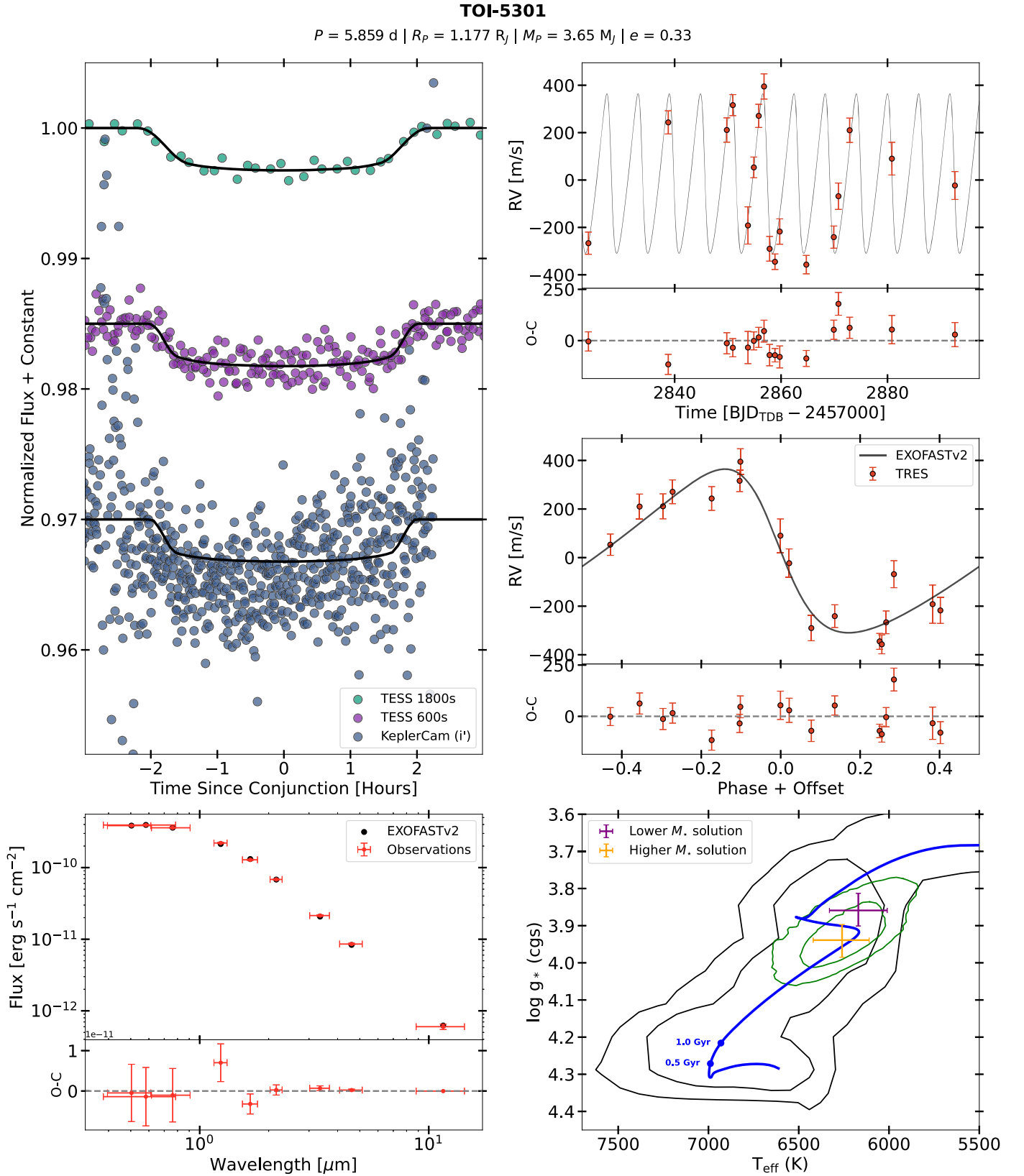
Figure 14. Same as Figure 6, but for TOI-5301. Similarly to Figure 10, TOI-5301 had a bimodal distribution of possible stellar masses, and we therefore represent the median and standard deviation of either solution in the bottom right panel.

the spectra of one star, TOI-5301, and found no evidence of an anomalous lithium enrichment that could be associated with youth or planetary engulfment. Each of these planets, however, will be an important member of the rising population of HJs that, once complete, will help answer the longest-standing question of exoplanet science, *how do HJs form and evolve?*

ORCID iDs

Jack Schulte ⓘ https://orcid.org/0000-0002-7382-0160
Joseph E. Rodriguez ⓘ https://orcid.org/0000-0001-8812-0565
Allyson Bieryla ⓘ https://orcid.org/0000-0001-6637-5401
Samuel N. Quinn ⓘ https://orcid.org/0000-0002-8964-8377
Karen A. Collins ⓘ https://orcid.org/0000-0001-6588-9574
Samuel W. Yee ⓘ https://orcid.org/0000-0001-7961-3907

Andrew C. Nine ⬤ https://orcid.org/0000-0002-6478-0611
Melinda Soares-Furtado ⬤ https://orcid.org/0000-0001-7493-7419
David W. Latham ⬤ https://orcid.org/0000-0001-9911-7388
Jason D. Eastman ⬤ https://orcid.org/0000-0003-3773-5142
Khalid Barkaoui ⬤ https://orcid.org/0000-0003-1464-9276
David R. Ciardi ⬤ https://orcid.org/0000-0002-5741-3047
Diana Dragomir ⬤ https://orcid.org/0000-0003-2313-467X
Mark E. Everett ⬤ https://orcid.org/0000-0002-0885-7215
Steven Giacalone ⬤ https://orcid.org/0000-0002-8965-3969
Ismael Mireles ⬤ https://orcid.org/0000-0002-4510-2268
Norio Narita ⬤ https://orcid.org/0000-0001-8511-2981
Avi Shporer ⬤ https://orcid.org/0000-0002-1836-3120
Ivan A. Strakhov ⬤ https://orcid.org/0000-0003-0647-6133
Stephanie Striegel ⬤ https://orcid.org/0009-0008-5145-0446
Martin Vaňko ⬤ https://orcid.org/0000-0002-2798-6944
Noah Vowell ⬤ https://orcid.org/0000-0002-0701-4005
Gavin Wang ⬤ https://orcid.org/0000-0003-3092-4418
Carl Ziegler ⬤ https://orcid.org/0000-0002-0619-7639
Paul Benni ⬤ https://orcid.org/0000-0001-6981-8722
Serge Bergeron ⬤ https://orcid.org/0000-0003-0846-1744
Henri M. J. Boffin ⬤ https://orcid.org/0000-0002-9486-4840
César Briceño ⬤ https://orcid.org/0000-0001-7124-4094
Catherine A. Clark ⬤ https://orcid.org/0000-0002-2361-5812
Kevin I. Collins ⬤ https://orcid.org/0000-0003-2781-3207
Jerome P. de Leon ⬤ https://orcid.org/0000-0002-6424-3410
Courtney D. Dressing ⬤ https://orcid.org/0000-0001-8189-0233
Phil Evans ⬤ https://orcid.org/0000-0002-5674-2404
Emma Esparza-Borges ⬤ https://orcid.org/0000-0002-2341-3233
Akihiko Fukui ⬤ https://orcid.org/0000-0002-4909-5763
Tianjun Gan ⬤ https://orcid.org/0000-0002-4503-9705
Ivan S. Gerasimov ⬤ https://orcid.org/0000-0001-7113-8152
Joel D. Hartman ⬤ https://orcid.org/0000-0001-8732-6166
Holden Gill ⬤ https://orcid.org/0000-0001-6171-7951
Keith Horne ⬤ https://orcid.org/0000-0003-1728-0304
Ferran Grau Horta ⬤ https://orcid.org/0000-0001-9927-7269
Steve B. Howell ⬤ https://orcid.org/0000-0002-2532-2853
Keisuke Isogai ⬤ https://orcid.org/0000-0002-6480-3799
Emmanuël Jehin ⬤ https://orcid.org/0000-0001-8923-488X
Jon M. Jenkins ⬤ https://orcid.org/0000-0002-4715-9460
Raine Karjalainen ⬤ https://orcid.org/0000-0002-2656-909X
John F. Kielkopf ⬤ https://orcid.org/0000-0003-0497-2651
Kathryn V. Lester ⬤ https://orcid.org/0000-0002-9903-9911
Colin Littlefield ⬤ https://orcid.org/0000-0001-7746-5795
Michael B. Lund ⬤ https://orcid.org/0000-0003-2527-1598
Andrew W. Mann ⬤ https://orcid.org/0000-0003-3654-1602
Mason McCormack ⬤ https://orcid.org/0000-0002-1463-9847
Enric Palle ⬤ https://orcid.org/0000-0003-0987-1593
Hannu Parviainen ⬤ https://orcid.org/0000-0001-5519-1391
David-Michael Peterson ⬤ https://orcid.org/0009-0009-1439-3101
Francisco J. Pozuelos ⬤ https://orcid.org/0000-0003-1572-7707
Zachary Raup ⬤ https://orcid.org/0000-0003-4278-6374
Phillip Reed ⬤ https://orcid.org/0000-0002-5005-1215
Howard M. Relles ⬤ https://orcid.org/0009-0009-5132-9520
George R. Ricker ⬤ https://orcid.org/0000-0003-2058-6662
Arjun B. Savel ⬤ https://orcid.org/0000-0002-2454-768X
Richard P. Schwarz ⬤ https://orcid.org/0000-0001-8227-1020
S. Seager ⬤ https://orcid.org/0000-0002-6892-6948

Ramotholo Sefako ⬤ https://orcid.org/0000-0003-3904-6754
Chris Stockdale ⬤ https://orcid.org/0000-0003-2163-1437
Mathilde Timmermans ⬤ https://orcid.org/0009-0008-2214-5039
Joshua N. Winn ⬤ https://orcid.org/0000-0002-4265-047X

References

Adams, F. C., & Laughlin, G. 2006, ApJ, 649, 1004
Astropy Collaboration, Price-Whelan, A. M., Sipőcz, B. M., et al. 2018, AJ, 156, 123
Astropy Collaboration, Robitaille, T. P., Tollerud, E. J., et al. 2013, A&A, 558, A33
Baranne, A., Queloz, D., Mayor, M., et al. 1996, A&AS, 119, 373
Batalha, N. M., Rowe, J. F., Gilliland, R. L., et al. 2010, ApJL, 713, L103
Batygin, K., Bodenheimer, P. H., & Laughlin, G. P. 2016, ApJ, 829, 114
Baudrand, J., & Bohm, T. 1992, A&A, 259, 711
Becker, J. C., Vanderburg, A., Adams, F. C., Rappaport, S. A., & Schwengeler, H. M. 2015, ApJL, 812, L18
Belokurov, V., Penoyre, Z., Oh, S., et al. 2020, MNRAS, 496, 1922
Boley, A. C., Granados Contreras, A. P., & Gladman, B. 2016, ApJL, 817, L17
Bonomo, A. S., Desidera, S., Benatti, S., et al. 2017, A&A, 602, A107
Brown, T. M., Baliber, N., Bianco, F. B., et al. 2013, PASP, 125, 1031
Bryan, M. L., Knutson, H. A., Howard, A. W., et al. 2016, ApJ, 821, 89
Buchhave, L. A., Bakos, G. Á, Hartman, J. D., et al. 2010, ApJ, 720, 1118
Buchhave, L. A., Latham, D. W., Johansen, A., et al. 2012, Natur, 486, 375
Buder, S., Sharma, S., Kos, J., et al. 2021, MNRAS, 506, 150
Caldwell, D. A., Tenenbaum, P., Twicken, J. D., et al. 2020, RNAAS, 4, 201
Chen, J., & Kipping, D. 2017, ApJ, 834, 17
Ciardi, D. R., Beichman, C. A., Horch, E. P., & Howell, S. B. 2015, ApJ, 805, 16
Collins, K. 2019, AAS, 233, 140.05
Collins, K., Quinn, S. N., Latham, D. W., et al. 2018, AAS, 231, 439.08
Collins, K. A., Kielkopf, J. F., Stassun, K. G., & Hessman, F. V. 2017, AJ, 153, 77
Cutri, R. M., Skrutskie, M. F., van Dyk, S., et al. 2003, VizieR Online Data Catalog: 2MASS All-Sky Catalog of Point Sources
Cutri, R. M., Wright, E. L., Conrow, T., et al. 2012, VizieR Online Data Catalog: WISE All-Sky Data Release
Dawson, R. I., & Johnson, J. A. 2018, ARA&A, 56, 175
De, K., MacLeod, M., Karambelkar, V., et al. 2023, Natur, 617, 55
Dekany, R., Roberts, J., Burruss, R., et al. 2013, ApJ, 776, 130
Donati, J. F., Semel, M., Carter, B. D., Rees, D. E., & Collier Cameron, A. 1997, MNRAS, 291, 658
Eastman, J. D., Rodriguez, J. E., Agol, E., et al. 2019, arXiv:1907.09480
Fabrycky, D., & Tremaine, S. 2007, ApJ, 669, 1298
Fűrész, G. 2008, PhD thesis, University of Szeged, Hungary
Fukui, A., Narita, N., Tristram, P. J., et al. 2011, PASJ, 63, 287
Furlan, E., Ciardi, D. R., Everett, M. E., et al. 2017, AJ, 153, 71
Furlan, E., & Howell, S. B. 2017, AJ, 154, 66
Gaia Collaboration, Brown, A. G. A., Vallenari, A., et al. 2021, A&A, 649, A1
Gaia Collaboration, Vallenari, A., Brown, A. G. A., et al. 2023, A&A, 674, A1
Garai, Z., Pribulla, T., Hambálek, Ľ., et al. 2017, AN, 338, 35
Gavel, D., Kupke, R., Dillon, D., et al. 2014, Proc. SPIE, 9148, 914805
Goldreich, P., & Tremaine, S. 1980, ApJ, 241, 425
Gray, D. F. 2005, The Observation and Analysis of Stellar Photospheres (Cambridge: Cambridge Univ. Press)
Guerrero, N. M., Seager, S., Huang, C. X., et al. 2021, ApJS, 254, 39
Halverson, S., Terrien, R., Mahadevan, S., et al. 2016, Proc. SPIE, 9908, 99086P
Harris, C. R., Millman, K. J., van der Walt, S. J., et al. 2020, Natur, 585, 357
Hayward, T. L., Brandl, B., Pirger, B., et al. 2001, PASP, 113, 105
Howell, S. B., Everett, M. E., Sherry, W., Horch, E., & Ciardi, D. R. 2011, AJ, 142, 19
Howell, S. B., Matson, R. A., Ciardi, D. R., et al. 2021, AJ, 161, 164
Huang, C., Wu, Y., & Triaud, A. H. M. J. 2016, ApJ, 825, 98
Huang, C. X. 2020a, TESS Lightcurves From The MIT Quick-Look Pipeline ("QLP") STScI/MAST, doi:10.17909/T9-R086-E880
Huang, C. X., Vanderburg, A., Pál, A., et al. 2020b, RNAAS, 4, 204
Huang, C. X., Vanderburg, A., Pál, A., et al. 2020c, RNAAS, 4, 206
Hunter, J. D. 2007, CSE, 9, 90
Ikwut-Ukwa, M., Rodriguez, J. E., Quinn, S. N., et al. 2022, AJ, 163, 9
Jeffries, R. D., Jackson, R. J., Wright, N. J., et al. 2023, MNRAS, 523, 802
Jehin, E., Gillon, M., Queloz, D., et al. 2011, Msngr, 145, 2
Jenkins, J. M., Caldwell, D. A., & Borucki, W. J. 2002, ApJ, 564, 495

Jenkins, J. M., Chandrasekaran, H., McCauliff, S. D., et al. 2010, Proc. SPIE, 7740, 77400D

Jenkins, J. M., Tenenbaum, P., Seader, S., et al. 2020, Kepler Data Processing Handbook: Transiting Planet Search, Kepler Science Document KSCI-19081-003

Jenkins, J. M., Twicken, J. D., McCauliff, S., et al. 2016, Proc. SPIE, 9913, 99133E

Jensen, E. 2013, Tapir: A web interface for transit/eclipse observability, Astrophysics Source Code Library, ascl:1306.007

Kabáth, P., Skarka, M., Sabotta, S., et al. 2020, PASP, 132, 035002

Knutson, H. A., Fulton, B. J., Montet, B. T., et al. 2014, ApJ, 785, 126

Koubský, P., Mayer, P., Čáp, J., et al. 2004, PAICz, 92, 37

Kozai, Y. 1962, AJ, 67, 591

Kunimoto, M., Huang, C., Tey, E., et al. 2021, RNAAS, 5, 234

Kupke, R., Gavel, D., Roskosi, C., et al. 2012, Proc. SPIE, 8447, 84473G

Kurucz, R. L. 1992, in IAU Symp. 149, The Stellar Populations of Galaxies, ed. B. Barbuy & A. Renzini (Dordrecht: Kluwer), 225

Lee, E. J., Chiang, E., & Ormel, C. W. 2014, ApJ, 797, 95

Lester, K. V., Matson, R. A., Howell, S. B., et al. 2021, AJ, 162, 75

Li, J., Tenenbaum, P., Twicken, J. D., et al. 2019, PASP, 131, 024506

Lidov, M. L. 1962, P&SS, 9, 719

Lightkurve Collaboration, Cardoso, J. V. D. M., Hedges, C., et al. 2018, Lightkurve: Kepler and TESS time series analysis in Python, Astrophysics Source Code Library, ascl:1812.013

Lin, D. N. C., & Papaloizou, J. 1986, ApJ, 307, 395

Lucy, L. B., & Sweeney, M. A. 1971, AJ, 76, 544

MAST 2021a, TESS Data Validation Files - All Single-Sectors, STScI/MAST, doi:10.17909/T9-2TC5-A751

MAST 2021b, TESS Light Curves - All Sectors, STScI/MAST, doi:10.17909/T9-NMC8-F686

Matson, R. A., Howell, S. B., Horch, E. P., & Everett, M. E. 2018, AJ, 156, 31

Mayor, M., & Queloz, D. 1995, Natur, 378, 355

McGurk, R., Rockosi, C., Gavel, D., et al. 2014, Proc. SPIE, 9148, 91483A

Montalbán, J., & Rebolo, R. 2002, A&A, 386, 1039

Mustill, A. J., Davies, M. B., & Johansen, A. 2015, ApJ, 808, 14

Naoz, S. 2016, ARA&A, 54, 441

Narita, N., Fukui, A., & Kusakabe, N., et al. 2015, JATIS, 1, 045001

Narita, N., Fukui, A., Kusakabe, N., et al. 2019, JATIS, 5, 015001

Ochsenbein, F., Bauer, P., & Marcout, J. 2000, A&AS, 143, 23

Paredes, L. A., Henry, T. J., Quinn, S. N., et al. 2021, AJ, 162, 176

Parviainen, H., Tingley, B., Deeg, H. J., et al. 2019, A&A, 630, A89

Paxton, B., Bildsten, L., Dotter, A., et al. 2011, ApJS, 192, 3

Paxton, B., Cantiello, M., Arras, P., et al. 2013, ApJS, 208, 4

Pepe, F., Mayor, M., Galland, F., et al. 2002, A&A, 388, 632

Poon, S. T. S., Nelson, R. P., & Coleman, G. A. L. 2021, MNRAS, 505, 2500

Pribulla, T., Garai, Z., Hambálek, L., et al. 2015, AN, 336, 682

Pych, W. 2004, PASP, 116, 148

Rafikov, R. R. 2005, ApJL, 621, L69

Rafikov, R. R. 2006, ApJ, 648, 666

Rasio, F. A., & Ford, E. B. 1996, Sci, 274, 954

Ricker, G. R., Winn, J. N., Vanderspek, R., et al. 2015, JATIS, 1, 014003

Rodriguez, J. E., Quinn, S. N., Huang, C. X., et al. 2019, AJ, 157, 191

Rodriguez, J. E., Quinn, S. N., Vanderburg, A., et al. 2023, MNRAS, 521, 2765

Rodriguez, J. E., Quinn, S. N., Zhou, G., et al. 2021, AJ, 161, 194

Safonov, B. S., Lysenko, P. A., & Dodin, A. V. 2017, AstL, 43, 344

Savel, A. B., Dressing, C. D., Hirsch, L. A., et al. 2020, AJ, 160, 287

Savel, A. B., Hirsch, L. A., Gill, H., Dressing, C. D., & Ciardi, D. R. 2022, PASP, 134, 124501

Schlafly, E. F., & Finkbeiner, D. P. 2011, ApJ, 737, 103

Schlegel, D. J., Finkbeiner, D. P., & Davis, M. 1998, ApJ, 500, 525

Schwab, C., Rakich, A., Gong, Q., et al. 2016, Proc. SPIE, 9908, 99087H

Schwarz, G. 1978, AnSta, 6, 461

Scott, N. J., Howell, S. B., Gnilka, C. L., et al. 2021, FrASS, 8, 138

Scott, N. J., Howell, S. B., Horch, E. P., & Everett, M. E. 2018, PASP, 130, 054502

Shallue, C. J., & Vanderburg, A. 2018, AJ, 155, 94

Skrutskie, M. F., Cutri, R. M., Stiening, R., et al. 2006, AJ, 131, 1163

Smalley, B., Anderson, D. R., Collier-Cameron, A., et al. 2012, A&A, 547, A61

Soares-Furtado, M., Cantiello, M., MacLeod, M., & Ness, M. K. 2021, AJ, 162, 273

Socrates, A., Katz, B., Dong, S., & Tremaine, S. 2012, ApJ, 750, 106

Stassun, K. G., Oelkers, R. J., Paegert, M., et al. 2019, AJ, 158, 138

Stassun, K. G., Oelkers, R. J., Pepper, J., et al. 2018, AJ, 156, 102

Strakhov, I. A., Safonov, B. S., & Cheryasov, D. V. 2023, AstBu, 78, 234

STScI 2022, TESS Calibrated Full Frame Images: All Sectors, STScI/MAST, doi:10.17909/0CP4-2J79

The pandas development Team 2023, pandas-dev/pandas: Pandas, Zenodo, doi:10.5281/zenodo.3509134

Tokovinin, A. 2018, PASP, 130, 035002

Tokovinin, A., Fischer, D. A., Bonati, M., et al. 2013, PASP, 125, 1336

Torres, G., Bakos, G. Á, Kovács, G., et al. 2007, ApJL, 666, L121

Twicken, J. D., Catanzarite, J. H., Clarke, B. D., et al. 2018, PASP, 130, 064502

Vanderburg, A., Becker, J. C., Buchhave, L. A., et al. 2017, AJ, 154, 237

Vanderburg, A., & Johnson, J. A. 2014, PASP, 126, 948

Vauclair, S. 1972, in IAU Colloq. 17: Age des Etoiles, ed. G Cayrel de Strobel & A. M. Delplace (Paris: Observatoire de Paris-Meudon), 38

Virtanen, P., Gommers, R., Oliphant, T. E., et al. 2020, NatMe, 17, 261

Wittenmyer, R. A., Clark, J. T., Trifonov, T., et al. 2022, AJ, 163, 82

Wizinowich, P., Acton, D. S., Shelton, C., et al. 2000, PASP, 112, 315

Wright, E. L., Eisenhardt, P. R. M., Mainzer, A. K., et al. 2010, AJ, 140, 1868

Yee, S. W., Winn, J. N., & Hartman, J. D. 2021, AJ, 162, 240

Yee, S. W., Winn, J. N., Hartman, J. D., et al. 2022, AJ, 164, 70

Yee, S. W., Winn, J. N., Hartman, J. D., et al. 2023, ApJS, 265, 1

Yoshida, S., Vissapragada, S., Latham, D. W., et al. 2023, AJ, 166, 181

Zhou, G., Quinn, S. N., Irwin, J., et al. 2021, AJ, 161, 2

Ziegler, C., Tokovinin, A., Briceño, C., et al. 2020, AJ, 159, 19

Zink, J. K., & Howard, A. W. 2023, ApJL, 956, L29